

NUMERICAL STUDY OF AN ELLIPSE PLAN HYPERBOLIC PARABOLOID CABLE-NET FRAME

Student
Bharat Kunwar

Supervisor
Dr Chris Williams

Department of Architecture and Civil Engineering



2011/12

AR40223

MEng Dissertation

Table of Contents

Abstract.....	i
Acknowledgements	ii
List of Symbols.....	iii
List of Figures	iv
List of Tables	iv
1 Introduction	1
2 Literature survey	3
2.1 Form Finding.....	3
2.2 Minimal Surfaces	3
2.3 Soap Films	4
2.4 Analytical Approach	4
2.5 Numerical Approach.....	5
2.5.1 Force Density Method.....	5
2.5.2 Dynamic Relaxation.....	5
2.5.3 Self-organising particle spring system	6
2.6 Case Studies	6
2.6.1 British Museum	6
2.6.2 Göteborg Scandinavium Arena	6
2.6.3 London Olympic Stadium	7
2.6.4 London Olympic Velodrome	8
2.7 Route to pursue.....	9
3 Model Development.....	10
3.1 Processing Integrated Development Environment.....	10
3.2 Definition of Geometry	10
3.2.1 Ellipse Plan Hyperbolic Paraboloid	10
3.3 Grid Layout	11
3.3.1 Boundary Truss	12
3.3.2 Cable-net Grid.....	12
3.3.3 Total Nodes and Members	14
3.3.4 The Nodes	14
3.3.5 The Members	14
3.3.6 Member length.....	15
3.4 Dynamic Relaxation Algorithm.....	17
3.4.1 From Strained to Unstrained Geometry	17
3.4.2 Stiffness of the nodes	18
3.4.3 Tension Coefficient	18
3.4.4 Forces at the nodes	18
3.4.5 Determining node velocity	19
3.4.6 Remapping the initial geometry.....	19
3.5 Sliding of cables.....	19

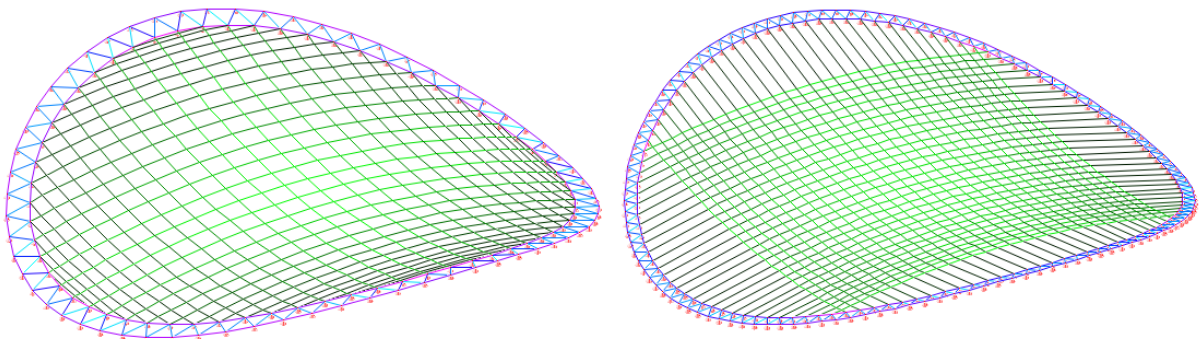
3.6	Cable pre-strain and resultant frame axial strain.....	20
4	Common Assumptions and Definitions	21
4.1	Material.....	21
4.2	Reference Frame.....	21
5	Results and Discussions	22
5.1	Test 1: Axial strain due to cable pre-strain and truss to cable x-sectional ratio	22
5.1.1	Aim of the test	22
5.1.2	Procedure.....	22
5.1.3	Results and Discussion.....	22
5.1.4	Limitations.....	25
5.2	Test 2: Axial strain due to cable pre-strain and the number of cables.....	26
5.2.1	Aim of the test	26
5.2.2	Procedure.....	26
5.2.3	Result and Discussion	26
5.2.4	Limitations.....	29
5.3	Test 3: Axial strain due to special case of cable arrangement	29
5.3.1	Aim of the test	29
5.3.2	Procedure.....	29
5.3.3	Result and Discussion	30
5.3.4	Limitations.....	32
6	Conclusion.....	33
6.1	Summary	33
6.1.1	Test 1: Axial strain due to cable pre-strain and truss to cable x-sectional ratio	33
6.1.2	Test 2: Axial strain due to cable pre-strain and the number of cables	33
6.1.3	Test 3: Axial strain due to special case of cable arrangement.....	33
6.2	Further Investigation	33
6.2.1	Effect of varying the elastic modulus of cable and truss material	33
6.2.2	Effect of varying aspect ratio and curvature ratio.....	34
6.2.3	Effect of loading the frame and temperature effects.....	34
6.2.4	Effect of pre-strain on maximum stresses experienced by the members.....	34
6.2.5	Comparison of the results with a physical model.....	34
6.3	Final Comments.....	34
Bibliography.....		35
Appendix		37
Note on result data.....		37
Note on source code.....		37

Abstract

This study investigates the behaviour of an ellipse plan cable-net hyperbolic paraboloid with a boundary. The numerical analysis uses a modified algorithm adapted from Alistair Day's dynamic relaxation algorithm. The modification to the algorithm allows for tracing an unknown initial geometry of a structure and an unknown final stress state from a known final geometry and a known initial stress state. This is significant, as is likely, if the final geometry is a critical aspect of the design brief from an engineering point of view.

The investigation attempts to determine the effect of pre-strain in the cables on the resultant axial strain by changing various parameters. The constituents of the geometry being investigated are: cable-net grid on an ellipse plan hyperbolic paraboloid surface bound by a triangulated truss boundary as visible in the diagram below. The boundary is supported vertically but it is free to move about horizontally in x and y-axis

It was found that increasing the truss to cable cross-sectional ratio of the frame gives a stiffer frame. A high truss to cable cross-sectional ratio fails due to limit imposed by cable cross sectional capacity and a low ratio fails due to limit imposed by truss cross sectional capacity. Increasing the number of cables embedded within the frame leads to a greater uniformity in force transfer, giving a stiffer frame. Restraining the cables at the intersection nodes also leads to a stiffer frame due to an even redistribution of initial pre-strain across all the cable members as the boundary shrinks. Finally, it was found that a special case of cable arrangement distinguished in the diagram below is stiffer, both when there are additional cables or the same number of cables per direction compared to an ordinary frame due to greater uniformity in transfer of forces to the boundary truss in the same way arches with uniformly distributed load deform less.



[Figure] Special m=16 (Left) vs. ordinary m=30 (Right) where the number of cables per direction are 30

Further areas of investigation proposed include understanding the effect of: varying truss and cable elastic moduli ratio; varying aspect ratio in x and y axis; varying frame curvature ratio in x, y and z axis; introducing dead and imposed load; incorporating thermal differences; cable pre-strain relationship with maximum stresses; and comparison with a physical model.

Acknowledgements

I want to thank my parents for their continual support throughout my studies.

I want to thank my supervisor Dr Chris Williams, who was always welcoming and helpful whenever I approached him for help or for new inspiration.

I want to thank Alex Kelly for all his input and the Java sessions.

I want to thank Kyla Darrell for all her support and patience.

I want to thank all my close friends for their constant encouragement.

List of Symbols

H	Mean curvature
\mathbf{R}^3	Three-dimensional Euclidian space
x_k	Displacement vector
\mathbf{g}_k	Gradient of x_k
W	Total potential energy
r	Radius of the hypar without scaling
a_i	Co-efficient to scale the radius r in i direction, $i = \{x, y\}$
b_i	Co-efficient to scale curvature of hypar in i direction, $i = \{x, y, z\}$
S_e	Arithmetic series
m	Number of cables per direction of the hypar of ellipse plan for the ordinary case
$m^&$	Number of cables per direction of the hypar of ellipse plan for the special case
n	Number of additional cables in each quarter for the special case
o	Number of special case additional members parallel to the boundary per quarter
$Nodes_{cable}$	Number of cable nodes
$Nodes'_{cable}$	Number of cable nodes for the special case
$Nodes_{truss}$	Number of boundary truss nodes
$Last Node$	Total number of cables nodes in the structure
$Members_{cable}$	Number of cable members
$Members'_{cable}$	Number of cables members for the special case
$Members_{truss}$	Number of boundary truss members
$Last Member$	Total number of members in the structure
X_{ij}	Final geometry co-ordinate for node i in j -axis, $j = \{x, y, z\}$
X'_{ij}	Initial geometry co-ordinate for node i in j -axis, $j = \{x, y, z\}$
Fix_{ij}	Restraining condition for node i in j -axis, $j = \{x, y, z\}$
End_{kl}	For member k, l refers to the node, $l = \{This\ End, That\ End\}$
EA_k	Product of elastic modulus and its x-sectional area for member k
T'_k	Pretension in member k
L'_k	Unstrained length of member k
T_k	Axial force in member k
L_k	Strained length of member k
σ_k	Stress in member k
E_k	Young's modulus (Elastic modulus) of member k
ε_k	Strain in member k
δL_k	Change in length of member k
F_k	Forces component of member k
F_{ij}	Sum of forces at node i in j -axis, $j = \{x, y, z\}$
K_i	Stiffness of node i
v_{ij}^t	Velocity of node i in j -axis, $j = \{x, y, z\}$ at time t
c	Velocity damping coefficient
ϕ	Angular interval for the outer boundary truss ring
θ	Offset to angular interval of the inner boundary truss ring
ω	Initial orientation angle for orthogonal grid of cable
l_i	Length of a member in the inner boundary truss ring
l_o	Length of a member in the outer boundary truss ring
r_i	Radius of the inner boundary truss ring
r_o	Radius of the outer boundary truss ring
δT_{cable}	Difference of initial pre-stress and effective tensile stress (slide case)
EA_{cable}	Product of cable Young's modulus and cable cross sectional area (slide case)
T_{cable}	Effective tensile stress (slide case)
T'_{cable}	Cable pre-stress (slide case)
E	Young's modulus
f_t	Tensile strength
f_c	Compressive strength
ε	Strain limit
$A_{truss}: A_{cable}$	Ratio of truss cross sectional area to cable cross sectional area
r_{cable}	Radius of the individual cables present in the frame
r_{truss}	Outer radius of the cross section of the boundary truss
t_{truss}	Thickness of the cross section of the boundary truss

$\varepsilon_{i,cables}$	Cable pre-strain
$\varepsilon_{i,frame}$	Frame axial strain
S_i	Ratio of $\varepsilon_{i,cables}$ to $\varepsilon_{i,frame}$
$L_{i,frame}$	Final, predefined span length of the frame
$L'_{i,frame}$	Initial, unknown span length of the frame
$T'_{i,cables}$	Total pre-stress force applied to the boundary truss by the cables

List of Figures

[Figure 2.1]	Frie Otto's Mannheim grid shell hanging chain model (Left) and Raleigh arena (Right)	3
[Figure 2.2]	Soap film surface with multiple boundaries	4
[Figure 2.3]	Catenoid	4
[Figure 2.4]	Göteborg Scandinavium Arena (Tibert, 1999)	7
[Figure 2.5]	London Olympic Stadium	8
[Figure 2.6]	London Olympic Velodrome	8
[Figure 3.1]	Plan view of ordinary case of cable layout where $m = 10, 15$ and 20 for (1), (2) and (3)	11
[Figure 3.2]	Plan view of special case cable layout when $m = 10$ for (4)	11
[Figure 3.3]	Isometric view of ordinary cable layout with definitions where $m = 10$	11
[Figure 3.4]	Velodrome roof cable layout	12
[Figure 3.5]	Definition of a typical member connecting nodes (This End) and (That End)	14
[Figure 3.6]	Definition of variables linked to the length of members	15
[Figure 3.7]	Boundary truss triangles that has been straightened out	16
[Figure 3.8]	Dynamic Relaxation Algorithm	17
[Figure 3.9]	London Olympic Stadium (Left) and London Olympic Velodrome (Right)	17
[Figure 3.10]	Pre-strained (unknown geometry) vs. defined final geometry (unknown stress)	17
[Figure 3.11]	Elevation of continuous cable members where $m = 3$	19
[Figure 3.12]	Plan view of frame deformation due to pre-strain	20
[Figure 4.1]	Anticlockwise: Plan, elevation and isometric view of the reference frame	21
[Figure 5.1]	Cable pre-strain (T'/EA) vs. axial strain (δ/L') for various Atruss:Acable ratio (Non-slide)	22
[Figure 5.2]	Cable pre-strain (T'/EA) vs. axial strain (δ/L') for various Atruss:Acable ratio (Slide)	23
[Figure 5.3]	$Si((T'/EA)/(\delta/L'))$ vs. cable pre-strain (T'/EA) for various Atruss:Acable ratio (Non-slide)	23
[Figure 5.4]	$Si((T'/EA)/(\delta/L'))$ vs. cable pre-strain (T'/EA) for various Atruss:Acable ratio (Slide)	24
[Figure 5.5]	$Si((T'/EA)/(\delta/L'))$ ratio vs. Atruss:Acable ratio	24
[Figure 5.6]	Slide (Left) vs. non-slide (Right) $m=25$ where (Max stress=Green, Min stress=Black)	25
[Figure 5.7]	Maximum and minimum slide Si /non-slide Si vs. Atruss:Acable ratio	25
[Figure 5.8]	Radius and radial ratio vs. m (Number of cables per direction)	26
[Figure 5.9]	Cable pre-strain (T'/EA) vs. axial strain (δ/L') for various m (Non-slide)	27
[Figure 5.10]	Cable pre-strain (T'/EA) vs. axial strain (δ/L') for various m (Slide)	27
[Figure 5.11]	$Si((T'/EA)/(\delta/L'))$ ratio vs. cable pre-strain (T'/EA) for various m (Non-slide)	27
[Figure 5.12]	$Si((T'/EA)/(\delta/L'))$ ratio vs. cable pre-strain (T'/EA) for various m (Slide)	28
[Figure 5.13]	$Si((T'/EA)/(\delta/L'))$ ratio vs. m	28
[Figure 5.14]	Maximum and minimum slide Si /non-slide Si vs. m	28
[Figure 5.15]	Number of cables vs. the total length of truss and cables and their ratios	29
[Figure 5.16]	Cable pre-strain (T'/EA) vs. axial strain (δ/L') for various m (Non-slide, Special case)	30
[Figure 5.17]	$Si((T'/EA)/(\delta/L'))$ ratio vs. cable pre-strain (T'/EA) for various m (Non-slide, Special)	30
[Figure 5.18]	$Si((T'/EA)/(\delta/L'))$ ratio vs. m (&Special case)	31
[Figure 5.19]	Special $m=40$ (Left) vs. ordinary $m=40$ (Right) where stress (Max =Green, Min =Black)	31
[Figure 5.20]	Force acting on boundary truss for the special (Left) and the ordinary (Right) case ($m=10$)	31
[Figure 5.21]	Special $m=16$ (Left) vs. ordinary $m=30$ (Right) where stress (Max =Green, Min =Black)	32
[Figure 5.22]	$Si((T'/EA)/(\delta/L'))$ ratio vs. actual number of cables (* refers to the special case)	32

List of Tables

[Table 3.1]	Known and unknown variables	18
[Table 4.1]	Material properties	21
[Table 4.2]	Properties of the frame to be used as a reference frame.....	21
[Table 5.1]	Table of x-sectional area ratio variables tested (*Reference frame)	22
[Table 5.2]	Change in outer radius with the change in number of cables (*Reference frame)	26
[Table 5.3]	Total length of truss and cables used and their ratios (* Reference frame, &Special case)	30

1 Introduction

Cable-nets, concrete shells and fabric structures are a family of membrane structures. They have been of growing interest in recent years, as they are associated with lightweight structures, which means materials are used efficiently. There are various methods and tools available to understand their behaviour.

An analytical basis of understanding, typically using differential geometry, has a steep learning curve, even for a competent engineer. Physical models using soap films, hanging chains, etc. are good for demonstrating and visualising the tangible behaviour. Numerical methods are often used for approaching the problem due to their versatility in terms of accommodating complex geometries defined by a set of logical conditions, which have greater resemblance to real life problems. However, numerical methods have a greater potential by allowing for structures to be simulated and tested in a virtual environment where precise measurements can be extracted to help understand the behaviour all the way up to a defined failure limit.

Form finding is a commonly used term to refer to the method of determining the shape of a membrane structures. With form finding, it is often the case that the final geometry of the structure is a result of the load and stress distribution that it is subject to.

While the numerical method of form finding makes it possible for the shape of the structure to be adjusted such that the final geometry tends closer to the desired shape, the question still remains whether it is possible to find the initial shape and the final stress distribution of the geometry if the initial stress distribution and the final geometry is known. If so, what initial shape has to be provided for the structure to come to the desired final shape?

This investigation will initially outline a review of literature to place the work in a historical context. Then, a selection of case studies of several construction projects that have implemented the use of membrane structures and/or form finding techniques will be reviewed.

The sequence of how the geometry being investigated came about will be described in the model development section. As the tests being conducted will be within a computational program, the nature of the calculations performed and the methods used in the program source code will be defined. The section will also attempt to state all the assumptions and simplifications made to make the tests feasible within the scope of this investigation. A modified version of Alistair Day's dynamic relaxation algorithm will also be explored within the model development section, which computes the initial geometry of the structure with a known stress state from the predefined final geometry of the structure with an unknown stress state.

The conditions that will govern the hyperbolic paraboloid cable net structure being explored will be: in plan, the boundary truss will follow the shape of an ellipse in a hyperbolic paraboloid plane; there will be cables that span from the nodes in the inner quarter of the boundary to the opposite quarter for the ordinary case of cable arrangement; there will be cables that span from the nodes in the inner half of the boundary to the opposite half for the special case of cable arrangement; and the boundary truss will only be supported vertically, and so is free to move about in the horizontal x and y axis, thus allowing for the perimeter to expand or contract depending on the forces acting on it.

The cables transfer forces to the boundary truss due to cable pre-strain causing axial displacement due to the lack of horizontal restraint. All tests will examine the axial strain of the frame due to the cable pre-strain applied and the influence on the derived initial geometry due to change in specific variables (detailed below). The computer program will output the results in numerical as well as graphical format for the variables, a selection of which will be used in the discussion.

The variables whose effects will be examined include: the ratio of the truss cross sectional area to the cable cross sectional area; the number of cables embedded within the frame; and a comparison of the special case of cable arrangement with the ordinary case of cable arrangement to determine which of the two is more efficient.

The differences in behaviour when the cables are allowed to slide over each other as opposed to being restrained at the intersection nodes will also be examined when the truss to cable cross sectional area ratios and the number of cables embedded within the frame vary.

This investigation hopes to provide a useful basis to inform a designer who is interested in designing a similar kind of roof structure, of the consequences of choosing the various possible routes. Graphical charts will be presented with experimental data represented in terms of dimensionless quantities where possible so that the information can be extracted and scaled to the required size.

The main limitation of this investigation is that the results will be presented for a specific configuration of geometry. Within the model environment, the examination of the slide behaviour will assume absence of friction to simplify the problem. The investigation will only cover the behaviour of a limited range of variables, which are best assumed remain valid within the range. A separate analysis would be required to establish the exact behaviour outside of the range.

Nevertheless, the outlined method would still be applicable to new situations. It would be possible to re-adapt the algorithm when the initial geometry and the final stress state needs to be determined for a membrane structure where the final geometry and the initial stress state are known.

2 Literature survey

In nature, plants and animals have evolved over millions of years to become efficient in their use of natural resources. Organisms have the capacity to repair themselves, decompose at the end of their lives and re-enter the ecological cycle. A tent is an ingenious invention that humans have produced allowing settlements to spread throughout the world (Otto & Rasch, 1995). Nomadic tribes still make use of them in areas where natural shelters are scarce. There is a paramount need to use the finite reserve of resources in the world sparingly. Biomimetics, term first coined by Otto H. Schmitt, has use in engineering to deal with resource scarcity. A good example this is form finding.

2.1 Form Finding

Form finding is a technique employed to produce lightweight structures, which could be described as naturally elegant, since they make an optimal use of materials with minimal mass (Otto & Rasch, 1995). It deals with finding the ideal deflected shape of a structure with a particular stress distribution.

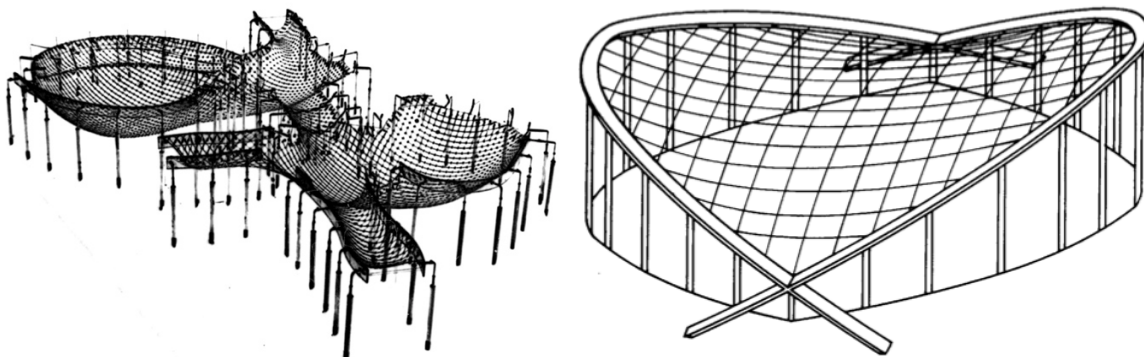


[Figure 2.1] Frie Otto's Mannheim grid shell hanging chain model (Left) and Raleigh arena (Right)

Gaudi and Frie Otto experimented with hanging chain models to find the optimal shape of compressive membrane structures. Frie Otto used nets made up of spring and rubber grid (Design Quarterly, 1969). Much of his work was creating the "maximum from the minimum" (Barnes, 1994). When a hanging chain model is inverted, the forces in the membrane are reversed and act in compression to become shell structures. They exhibit minimised bending moment like the hanging chain models. Fabric and cable-net structures also behave purely by membrane tensile action. More recently, saddle shaped shell structures and orthogonal cable-net structures like the Raleigh arena are emerging worldwide (Berger, 1996). In general, the problems with membrane structures are often congruent to that of minimal surfaces.

2.2 Minimal Surfaces

Minimal surfaces are described as surfaces with a mean curvature of zero (Struik, 1961). Mean curvature H can be written as,

$$H = \frac{(k_1 + k_2)}{2} = 0$$

[Equation 2.1]

In [Equation 2.1], as explained by (Plateau, 1873), $k_1 = 1/r_1$, $k_2 = 1/r_2$ are the principal curvatures and r_1 and r_2 are the corresponding radii. Minimal surfaces have the attribute of a locally minimised area giving the overall surface the smallest area for a given boundary condition. Soap films demonstrate this when a closed wire is dipped into a soap solution and then taken out (Colding & Minicozzi, 2006).

2.3 Soap Films

Soap film membranes are made up of liquids, which form when a non-intersecting closed loop of desired shape is dipped into a membrane-forming liquid and then taken out. The primary driving factor for research behind soap film has been to establish what the different forms of possible surfaces are and why they are possible. The best-known membrane-forming liquid is soap lye. The structure is very thin. It is prestressed, flexurally non-rigid and only bears axial load (Otto & Rasch, 1995). The given shape is also in a state of static equilibrium.

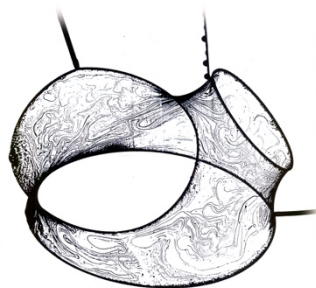


[Figure 2.2] Soap film surface with multiple boundaries

The first documented experiments by (Plateau, 1873) proposed that soap films could be used to visualise minimal surfaces. They have been the traditional tools to demonstrate various minimal surfaces but the knowledge gap is closing with numerous examples demonstrated mathematically, some of which are difficult to achieve using soap film alone. This is normally the case for unstable minimal surfaces, when the genus is higher than zero. To clarify the concept of genus, a sphere has a genus of zero; a torus has a genus of one and so on. Torus, an unstable surface, is visually demonstrated by (Noddy, 2004) on his website. A soap film with a non-intersecting boundary provides a stable surface. A sphere is the only unbound shape with stable equilibrium. However, for an engineering purpose, a boundary is required and the structure needs to be stable.

2.4 Analytical Approach

An analytical approach to examination of surfaces requires an in depth understanding of differential geometry with a fairly steep learning curve. However topics relevant to form finding are briefly outlined.

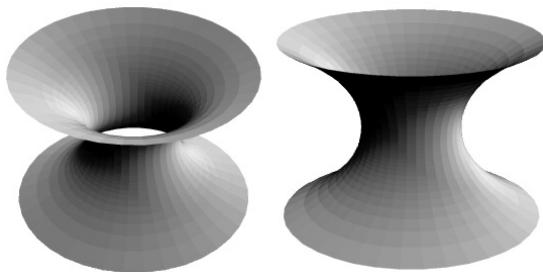


[Figure 2.3] Catenoid

Catenoid [Figure 2.3] was the first non-trivial minimal surface identified by Euler in 1740s and explained by Lagrange in 1760s using differential geometry. A generic non-parametric minimal surface with co-ordinates of the surface on a three-dimensional Euclidian space (\mathbf{R}^3) is given by $(x, y, f(x, y))$. For such a configuration, the Euler-Lagrange equation is given by [Equation 2.2] where f_i is the partial derivative with respect to i (Osserman, 1986).

$$(1 + f_y^2)f_{xx} + (1 + f_x^2)f_{yy} - 2f_x f_y f_{xy} = 0$$

[Equation 2.2]

A two dimensional surface that is characterised by parameters in \mathbf{R}^3 (Spivak, 1999) can be written as $(x(u, v), y(u, v), z(u, v))$ where x, y and z are functions of u and v to determine the various co-ordinates of the surface.

2.5 Numerical Approach

Development in numerical methods of form finding has taken several routes. The problem in all cases is the question of how the prescribed stress distribution can be applied within a given boundary condition; this introduces an inverse mathematical problem (Bletzinger, Wuchner, Daoud, & Camprubi, 1998). This contrasts with standard calculations in mechanics where the structural deformation of the object determines the stress distribution in the object. Different parties have developed different procedures and algorithms, each with their own strengths and weaknesses, discussed as follows.

2.5.1 Force Density Method

Force density method is one of the earliest numerical form-finding techniques introduced by (Scheck, 1974) and developed by (Osserman, 1986). This relatively simple method is applicable in various forms of cable-net structures but is very useful for structures with compression members (Tibert, 1999). The technique was further developed by (Lewis W. J., 2003) in response to the modelling requirements of certain elements of the Munich Olympic complex. The non-linear problem of form finding of cable-net structures is linearized by this method. It is fold-over free as demonstrated by (Southern, 2011) because such a configuration would not be in a state of equilibrium. This method of form finding is also suitable for generating cutting patterns rapidly due to its simple formulation (Tibert, 1999).

2.5.2 Dynamic Relaxation

Dynamic relaxation is a computational method developed to find geometry of lightweight tension structures, consisting of pre-stressed cable-nets and fabric membranes. Earliest version using simplified Verlet algorithm was described by (Day, 1965). Programming languages such as Fortran have been used to generate the initial surface topology and undertake post processing of data by (Lewis & Lewis, 1996) using dynamic relaxation algorithm as a solver for the resulting non-linear system of equilibrium equations. By using the principle of minimising the potential energy of surface tension indirectly, i.e. focusing on the nodes where the kinetic energy is high, it derives the optimal shape of tension membranes.

Direct minimisation of potential energy with respect to displacement has been demonstrated (Zhang & Tabarrok, 1999). Total potential energy W has been minimised by incorporating the Newton-Raphson method (Buchholdt, 1999). By supposing that the change in the displacement vector at the end of the k^{th} iteration is δx_k , the gradients of position vector x_k and x_{k+1} are given by,

$$\mathbf{g}_k = \frac{\delta W}{\delta x_k}$$

[Equation 2.3]

$$\mathbf{g}_{k+1} = \frac{\delta W}{\delta x_{k+1}}$$

[Equation 2.4]

This method depends on whether the elimination of higher order terms in Taylor series is justified. Incorporating the stiffness matrix \mathbf{K} and expanding using Taylor series,

$$\delta x_k = -\mathbf{K}_k^{-1} \mathbf{g}_k$$

[Equation 2.5]

$$x_{k+1} = x_k + \delta x_k$$

[Equation 2.6]

2.5.3 Self-organising particle spring system

Recent developments in computational form finding have led to a system of self-organising particle spring system. Using Delaunay triangulation algorithm, triply periodic minimal surfaces were simulated by (Tenu, 2009) to determine an efficient topology made up of one standard length. This was in order to prescribe standard sizes for fabrication components. As opposed to dynamic relaxation, this method allows for creation of minimal surfaces that do not start with a predefined topology. It is based on a growth algorithm. Nodes are added according to the geometrical constraints and the subdivision rules are applied. As this method is still at its infancy, there is a potential for improvement by developing a more advanced parametric design tool that takes more variables into account during the surface generation process.

2.6 Case Studies

All structural and architectural projects have their own unique constraints according to (Williams, 2003). As a way of drawing inspiration, interesting features of some grid shell and cable net structures are discussed below with special attention to the overview of mechanism behind their function and the palette of materials used in their construction.

2.6.1 British Museum

The British Museum great court roof covers a rectangular area of 70x100m², which contains a 44m diameter reading room. The roof construction is characterised by a grid of intersecting triangles, composed of steel members welded at the nodes, providing structural stiffness. One flat panel of double-glazing is used for each triangle of the structural grid. The internal circular reading room and the external rectangular boundary are the geometric constraints. The roof is not allowed to apply any lateral thrust to the existing historic buildings around the rectangular perimeter. Lateral thrusts may only be applied at the corners where it can be resisted by tension in the edge beam resolving the external forces internally (Williams, 2001). Both analytical and numerical methods were used to derive the geometry of the roof. This provides a good precedence to how membrane structures are analysed in real world applications.

2.6.2 Göteborg Scandinavium Arena

Göteborg Scandinavium Arena [Figure 2.4] is a building that was the largest covered arena in northern Europe when it was completed in 1971. With room for 14,000 spectators, the roof of the arena consists of thermal and water insulation cladding laid out on a pre-stressed cable net. All cables span between reinforced concrete ring supported by 4 stiff pylons and 40 circular concrete columns. The roof surface closely resembles a hyperbolic paraboloid. The cables rise 10m to the summit and fall 4m to the

valley of the surface in relation to the centre. The cable spacing is 4m, and is more or less even in both directions. The rectangular concrete ring beam has a width of 3.5m and a height of 1.2m. As for the in-situ cast circular columns, they are mainly designed to withstand axial forces. The radially orientated pylons are stiffer elements designed to take large horizontal forces from the roof due to imposed loads.

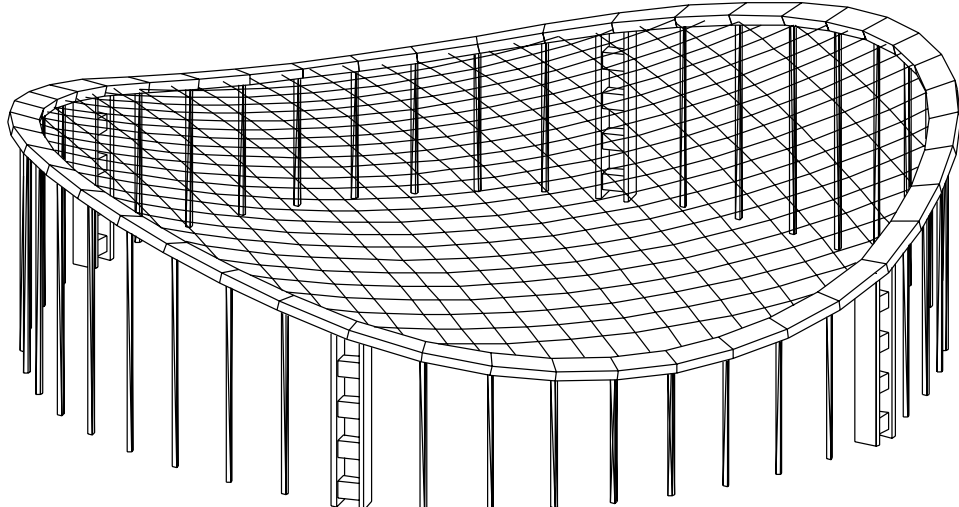


[Figure 2.4] Göteborg Scandinavium Arena (Tibert, 1999)

A detailed thesis of cable roof structures by (Tibert, 1999) provides an essential overview of numerical analysis of cable-net structures, with an example demonstrating the finite element analysis of the Scandinavium Arena. The findings of the thesis explain that the bending moments in the supporting concrete ring beam was very sensitive to the overall shape due to large inconsistency in bending moment distribution between the analyses. Also, a simplified method presented agrees well with the more accurate finite element calculations.

While columns are predominantly acting axially to take vertical loads, to what extent are the pylons resisting the horizontal loads? Would the boundary support have a greater material efficiency if they were able to displace freely in the horizontal plane by reducing the need for stiff pylons? This presents a potential route for further investigation.

2.6.3 London Olympic Stadium

The Olympic Stadium [Figure 2.5] roof supports the fabric roof structure and the 112 black steel rakers act as the terracing supports for the 55000 upper tier seats. The 28 sections of roof compression truss, each weighing 85 tonnes, are 30m wide and 15m high, and are able to expand and contract independently of the rest of the structure due to thermal effects and imposed loads. There are 4500 reinforced concrete columns installed as foundations and 12000 pre-cast concrete terracing for the lower tier seating.

The lack of stiff support and mechanism that allows for the perimeter of the roof to move independently of the rest of the stadium structure gives it a lightweight appearance. This is in contrast to structures with stiff boundaries. Could this form of support be superimposed with the hyperbolic paraboloid structure presented for the Göteborg Scandinavium Arena?

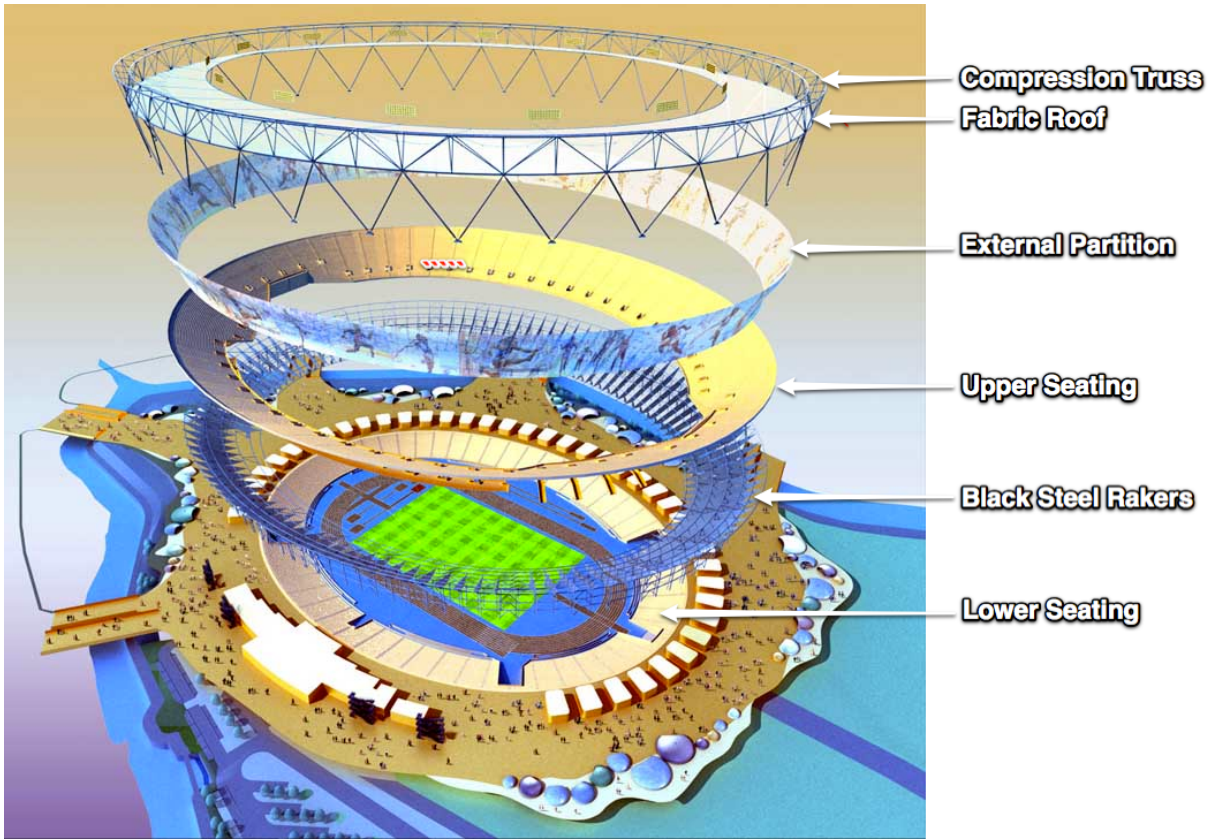


[Figure 2.5] London Olympic Stadium

2.6.4 London Olympic Velodrome

The Olympic Velodrome is a new addition to the family of buildings that utilises the geometric advantages of minimal surfaces (Olympic Delivery Authority, 2011). It features a double curvature roof [Figure 2.6], which is not strictly a minimal surface, but is a good approximation as shown by (Clarke, 2011). Although a catenary is the true representation of a minimal surface, the roof uses an approximate parabolic function to derive its geometry.



[Figure 2.6] London Olympic Velodrome

The roof reflects the geometry of the indoor cycling track. The indoor 6,000 seating facility is split up into two tiers, with a 360-degree concourse level in between them. The double curvature roof features strategically placed roof lights that provide natural daylight reducing the need for artificial lighting. It utilises a cable-net roof structure that is 12,000 m² in area and a total cabling of 16km.

Following excavation of 48000 m³ of material from the site, more than 900 piles were driven up to 26m beneath the ground to complete the foundation work and around 2,500 sections of steelwork installation complete the structure.

The roof has a stiff support structure around the boundary that more or less restricts horizontal as well as movement. The double curvature roof behaves in such a way that when it is strained in the warp direction due to imposed loads, the weft direction curves inwards and vice versa. This geometry gives the overall roof structure an effect of bending stiffness.

With the 2012 Olympics fast approaching at the time of writing this report, this structure is an option to explore further by changing the parameter of various components and observing the change in behaviour, which could help identify potential improvements that could be made to the current design.

2.7 Route to pursue

Various methods of form finding have been identified and elaborated. Various case studies have also been looked at to seek inspiration. As a result, the problem being investigated will be to analyse the behaviour of a cable-net roof structure inspired by combinations of aspects of the case studies that have been looked at. As a relatively new construction, the Olympic Velodrome is an interesting structure that would benefit from a re-examination of how it would perform if some of the variables that define the constituent components were changed.

The conditions that will govern the hyperbolic paraboloid cable net structure being explored will be: in plan, the boundary truss will follow the shape of an ellipse in a hyperbolic paraboloid plane; there will be cables that span from the nodes in the inner quarter of the boundary to the opposite quarter for the ordinary case of cable arrangement; there will be cables that span from the nodes in the inner half of the boundary to the opposite half for the special case of cable arrangement; and the boundary truss will only be supported vertically, but will be free to move about in the horizontal x and y axis, allowing for the perimeter to expand or contract depending on the forces acting on it.

Taking the direction of using a numerical method using dynamic relaxation algorithm due to its versatility, a computer program will be written to perform the analysis. Such a computer program would provide a greater degree of flexibility in terms of specifying the variables whose effects are being examined. The algorithm will support tensile and compression members in order to allow for both the cable net and the boundary truss assuming linear elastic behaviour in the members. The program will measure the axial strain of the frame due to pre-strain in the cable.

Rotational stiffness in potential rigid connections will be ignored. The nodes connecting the members in the boundary truss will be pinned connections as a way of simplifying the problem further as allowing for an additional rotational DOF presents greater complexity in the calculations.

3 Model Development

3.1 Processing Integrated Development Environment

The model is developed in a programming environment called Processing. Processing is based on the Java programming language. Developed by MIT, the simplified syntaxes and the ease of interface with graphical outputting have lead to its increased popularity in the recent years. The advantage of being able to visualise the output in real time serves to help determine the failure mechanism of the structure being tested under varying parameters, therefore useful for engineering purposes. There are other software development environments available for computational analysis but the choice is also influenced by existing familiarity with the environment.

3.2 Definition of Geometry

The Velodrome built for the London 2012 Olympic games, inspires the geometry of the structure that will be investigated here. The geometry is that of a hyperbolic paraboloid or “hypar” with an ellipse plan boundary. In reality, a hypar is an infinite surface in a three dimensional space. There are different ways to express it using parametric equations. It is necessary for our purpose to define a boundary, which in this case is an ellipse in plan due to the designer’s intent to make the shape of the Velodrome roof follow the geometry of the indoor cycling track.

3.2.1 Ellipse Plan Hyperbolic Paraboloid

In an x-y plane, an ellipse is defined by the modified equation for a circle within a polar co-ordinate system as given by [Equation 3.1]. In the equation, a_i where the index values for $i = \{x, y\}$, is the constant that scales the radius r in x and y axis, provided that the condition $0 < a_i \leq 1$ is met. When all the values of a_i are equal to each other, it is a circle, a special case of an ellipse. As for the variables r and θ , the conditions that $r > 0$ and $0 \leq \theta \leq 2\pi$ apply.

$$\begin{aligned}x &= a_x r \sin \theta \\y &= a_y r \cos \theta\end{aligned}$$

[Equation 3.1]

$$\frac{z}{b_z} = \frac{y^2}{b_y^2} - \frac{x^2}{b_x^2}$$

[Equation 3.2]

On the other hand, a hypar is a doubly curved surface and is a function of x and y co-ordinates in a 3D Euclidean space. In [Equation 3.2], b_i is the constant that scales the curvature of the hypar surface in the direction given by the index $i = \{x, y, z\}$, provided that the condition $b_i > 0$ is met.

A 2D elliptical boundary can be projected in 3D space, where the location of the co-ordinates in the z-axis is a function of the position of the co-ordinates in the x and y-axis. Since the x and y co-ordinates of the ellipse boundary are known, the position of any of those co-ordinates in the z-axis can be determined by plugging in the co-ordinates from the ellipse equation in [Equation 3.1]. Substituting into [Equation 3.2], we get,

$$\frac{z}{b_z} = \frac{(a_y r \cos \theta)^2}{b_y^2} - \frac{(a_x r \sin \theta)^2}{b_x^2}$$

[Equation 3.3]

3.3 Grid Layout

The Velodrome roof constitutes an arrangement of a boundary truss and a series of cables embedded within the boundary. The triangulated truss lies along the perimeter of the ellipse boundary. It is modelled as a pin jointed truss to negate the problem of dealing with moments and to simplify the problem. In reality, the joints are rigid but with trusses, the majority of the forces are transferred axially and moment resistance provides little contribution to structural rigidity (Seward, 2003).

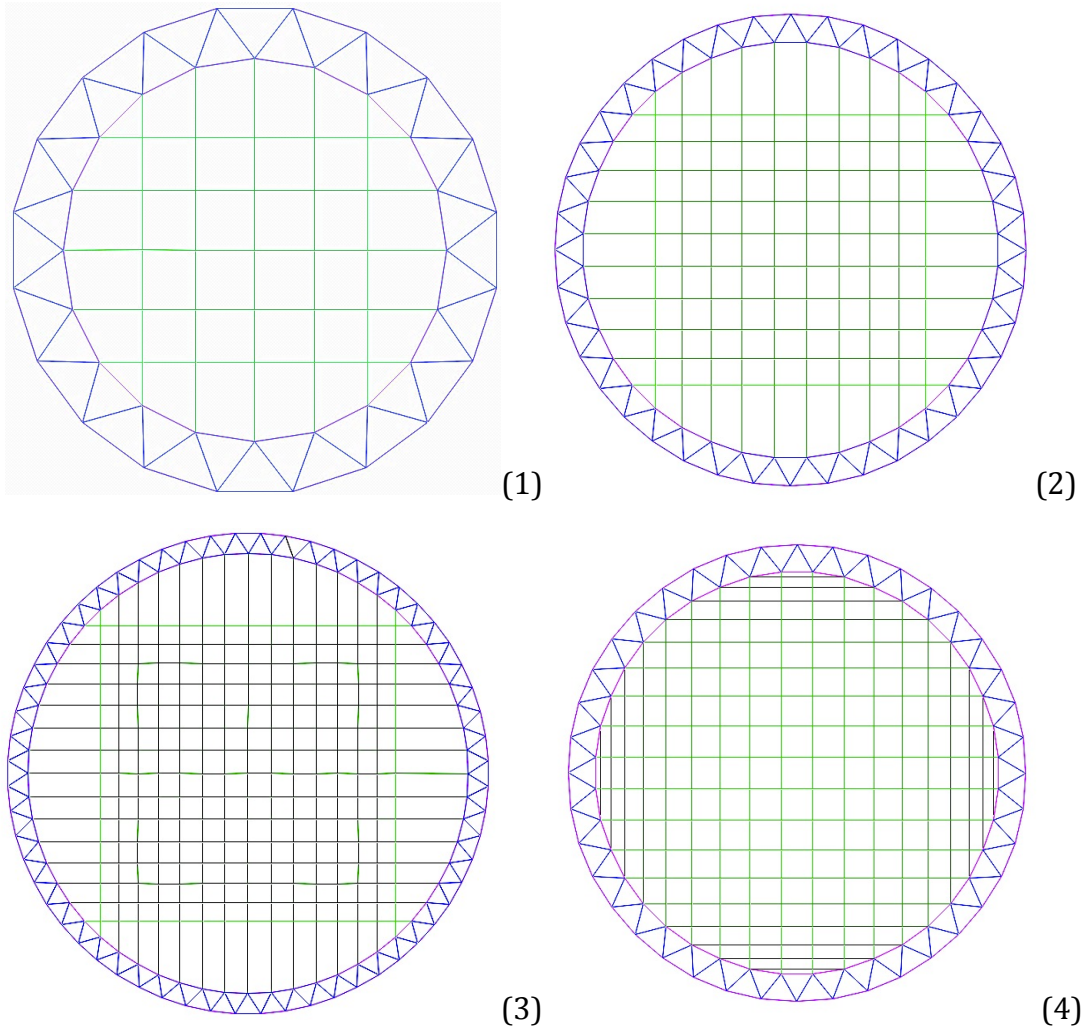


[Figure 3.1] Plan view of ordinary case of cable layout where $m = 10, 15$ and 20 for (1), (2) and (3)

[Figure 3.2] Plan view of special case cable layout when $m = 10$ for (4)

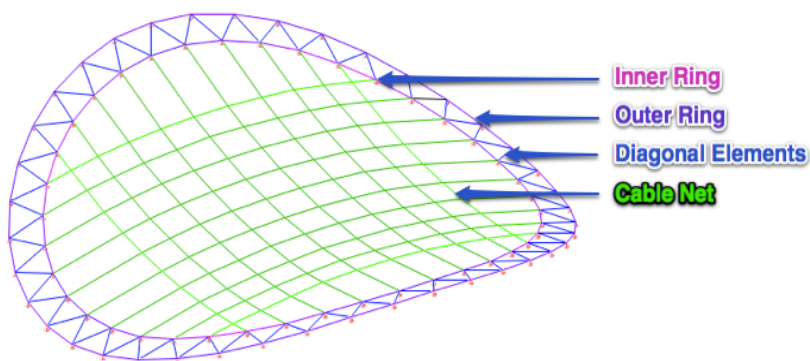


[Figure 3.3] Isometric view of ordinary cable layout with definitions where $m = 10$

The ellipse boundary is divided up into four quarters. Variable m defines the number of cables that connect between the inner ring nodes from one quarter to the opposite quarter in the two directions. Nodes are formed where the cables intersect. For diagrams labelled 1, 2 and 3 in [Figure 3.1], $m = 5, 10$ and 15 respectively.

3.3.1 Boundary Truss

The boundary truss is effectively a Warren truss that wraps around the perimeter. The node co-ordinates are located on the ellipse plan hyperbolic paraboloid surface given by [Equation 3.3]. The nodes in the inner ring and the outer ring as shown in [Figure 3.3] give the total number of truss nodes. The total number of truss nodes is given by [Equation 3.4].

$$Nodes_{truss} = 4(2m) = 8m$$

[Equation 3.4]

There are twice as many truss members as there are truss nodes, visible in [Figure 3.3]. The total number of members in the inner ring, the outer ring and the diagonal elements that connect nodes between the inner and the outer ring is given by [Equation 3.5].

$$Members_{truss} = 4(4m) = 16m$$

[Equation 3.5]

3.3.2 Cable-net Grid

There are a number of ways that the cable-net grid may be set out depending on the design brief. It is possible to have evenly spaced cables in order to allow for insulations panels of uniform dimensions to be manufactured with the exception of the boundary panels. However, this introduces the complexity around the boundary where the cable end conditions change as we follow the swerve of the truss. In [Figure 3.4], the opaque and transparent roof panels, both of which have different dimensions, govern the cable-net grid of the Velodrome roof. Apart from these issues, a uniform grid is also difficult to code without enabling support for accounting for rotational stiffness at the nodes.

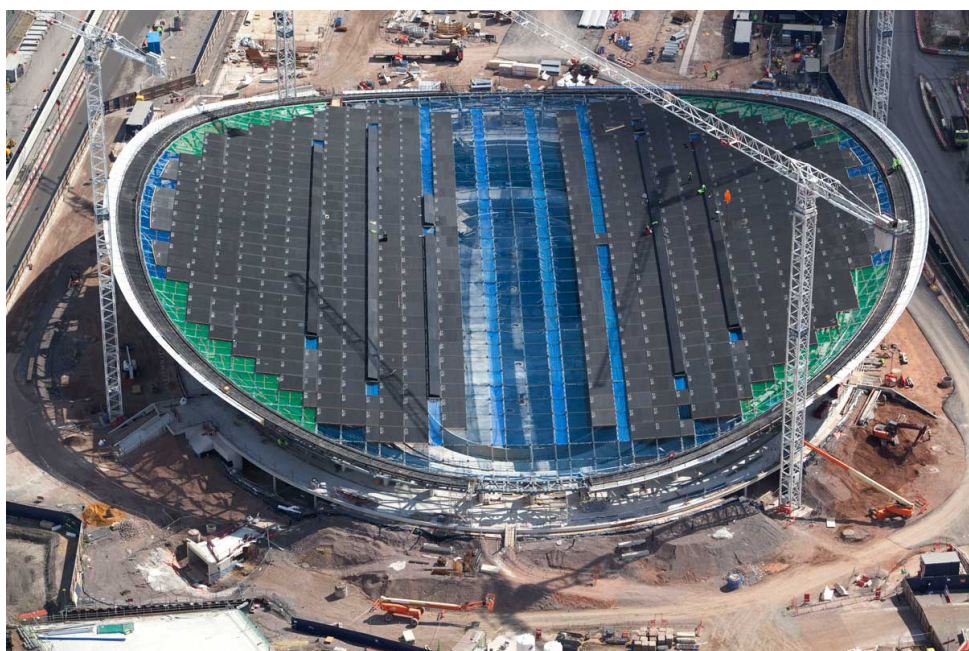


[Figure 3.4] Velodrome roof cable layout

To keep matters simple, the grid layout is determined by the dimensions of the truss around the perimeter. As m increases, the cable-net layout increases in complexity with more intersections, therefore forming more nodes and members.

For the ordinary case of cable arrangement shown in [Figure 3.1], the total number of nodes is given by [Equation 3.6].

$$Nodes_{cable} = m^2$$

[Equation 3.6]

For the special case of cable layout shown in [Figure 3.2], additional cables continue to connect all the inner ring nodes from one half of the ellipse plan boundary to the opposite half, introducing additional cable nodes. As the number of members per cable tangent to the boundary reduces in number as the boundary is approached, the total number of nodes is derived using the arithmetic series equation given by [Equation 3.7].

$$S_e = \frac{n}{2}(a_1 + a_n)$$

[Equation 3.7]

Using [Equation 3.7], the total number of additional nodes required is given by [Equation 3.8] where $n = \frac{m}{2}$ if m is even or $n = \frac{m-1}{2}$ if m is odd. For this arrangement, the number of nodes decreases by two as the boundary is approached and the number of intersection points for the cable closest to the boundary is given by $m - 2n$. Therefore, the first term $a_1 = 2$ and the last term $a_n = 2n$.

$$Nodes'_{cable} = 4\left(mn - \frac{n}{2}(2 + 2n)\right) = 4n(m - n - 1)$$

[Equation 3.8]

For the ordinary case of cable arrangement, the cable members span between the boundary truss nodes in a grid-like manner. By inspection, the total number of cable members is given by [Equation 3.9].

$$Members_{cable} = 2m(m + 1)$$

[Equation 3.9]

For the special case, in the direction normal to the edge, the same number of additional members is required as the additional nodes given by [Equation 3.8]. Tangent to the edge, the additional members required are quantified using the arithmetic series equation in [Equation 3.7], where the additional number of cables in each quarter is quantified by $o = \frac{m-2}{2}$ if m is even and $o = \frac{m-1}{2}$ if m is odd. Therefore, the total number of additional cable members is given by [Equation 3.10].

$$\begin{aligned} Members'_{cable} &= 4\left(om + \frac{o}{2}(1 + 2o - 1)\right) + 4\left(mn - \frac{n}{2}(2 + 2n)\right) \\ &= 4o(m + o) + 4n(m - n - 1) \end{aligned}$$

[Equation 3.10]

3.3.3 Total Nodes and Members

The total number of nodes and members put together from the cable and truss elements is given by [Equation 3.11] and [Equation 3.12] respectively except for the ordinary case of cable arrangement where the nodes and members for the special case of cable arrangement would be excluded.

$$\begin{aligned} \text{Last Node} &= \sum \text{Node} = \text{Node}_{\text{truss}} + \text{Node}_{\text{cable}} + \text{Node}'_{\text{cable}} \\ &= m^2 + 8m + 4n(m - n - 1) \end{aligned}$$

[Equation 3.11]

$$\begin{aligned} \text{Last Member} &= \sum \text{Member} = \text{Member}_{\text{truss}} + \text{Member}_{\text{cable}} + \text{Member}'_{\text{cable}} \\ &= 2m(m + 8) + 16m + 4o(m + o) + 4n(m - n - 1) \end{aligned}$$

[Equation 3.12]

3.3.4 The Nodes

The nodes are characterised by x, y and z co-ordinates in space. It is necessary to define for reference and to assign nodal properties. It constitutes of a multidimensional array with two indices where i corresponds to the node number and j corresponds to the axis being referred given by [Equation 3.13]. The known final geometry is X_{ij} and the unknown initial geometry is X'_{ij} but is preliminary assigned the same nodes.

$$X_{ij} = X'_{ij} = \{\text{Coordinate}\} \text{ where } i = \{1 \dots \text{Last Node}\}, j = \{x, y, z\}$$

[Equation 3.13]

Each node has three DOFs in x, y and z direction but some nodes are restrained in some or all directions, i.e. the truss nodes are fixed vertically and initially restrained in both horizontal directions. This is controlled by another matrix with two indices,

$$Fix_{ij} = \{\text{True, False}\} \text{ where } i = \{1 \dots \text{Last Node}\}, j = \{x, y, z\}$$

[Equation 3.14]

3.3.5 The Members

The members describe how the nodes are connected. Each member has two ends, each of which corresponds to a node number, as shown in [Figure 3.5].

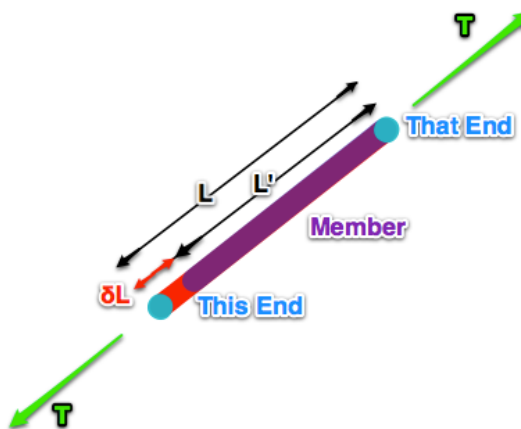


[Figure 3.5] Definition of a typical member connecting nodes (This End) and (That End)

The ends are described by matrix End_{kl} with two indices. Each member has a constant EA_k (product of young's modulus and cross-sectional area), T'_k (pretension) and L'_k (unstrained length) written as follows,

$$End_{kl} = \{1 \dots Last\ Node\} \text{ where } k = \{1 \dots Last\ Member\} \text{ and } l = \{This\ End, That\ End\}$$

[Equation 3.15]

$$EA_k \text{ where } k = \{1 \dots Last\ Member\}$$

[Equation 3.16]

$$T'_k \text{ where } k = \{1 \dots Last\ Member\}$$

[Equation 3.17]

$$L'_k \text{ where } k = \{1 \dots Last\ Member\}$$

[Equation 3.18]

3.3.6 Member length

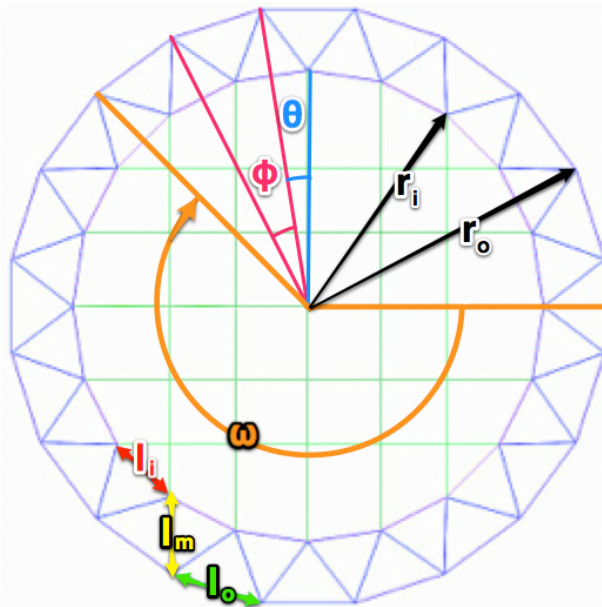


[Figure 3.6] Definition of variables linked to the length of members

For the sake of argument, the inner triangles of the boundary truss are assumed to be roughly equilateral. For grid alignment, the highest peak and the lowest valley of the hypar are perpendicular to the direction of the cables spanning across two directions. The orientation angle ω given by [Equation 3.19] is shown in [Figure 3.6] and enables the cables in the frame to be aligned in an orthogonal grid in plan view.

$$\omega = \pi + \frac{\pi}{4} + \theta = \frac{\pi}{4} \left(5 + \frac{1}{m} \right)$$

[Equation 3.19]

The first truss node in the outer ring is positioned at an orientation angle ω . Similarly, the first truss node in the inner ring is positioned at angle $\omega + \theta$, where θ , a function of m , is an intermediate angle given by [Equation 3.20]. The subsequent outer and inner ring nodes are both located at an angle interval of φ , also a function of m and described by [Equation 3.21].

$$\theta = \frac{\pi}{4m}$$

[Equation 3.20]

$$\varphi = \frac{\pi}{2m}$$

[Equation 3.21]

The distances between the nodes in the truss inner and outer ring give the length of members in the respective rings. The distances between the outer ring nodes and the offset inner ring nodes give the length of the interconnecting diagonal truss members. Using [Equation 3.21], the length of truss elements l_i and l_o as indicated in [Figure 3.6] are given by [Equation 3.22] and [Equation 3.23] respectively.

$$l_i = \varphi \cdot r_i = \frac{\pi}{2m} r_i$$

[Equation 3.22]

$$l_o = \varphi \cdot r_o = \frac{\pi}{2m} r_o$$

[Equation 3.23]

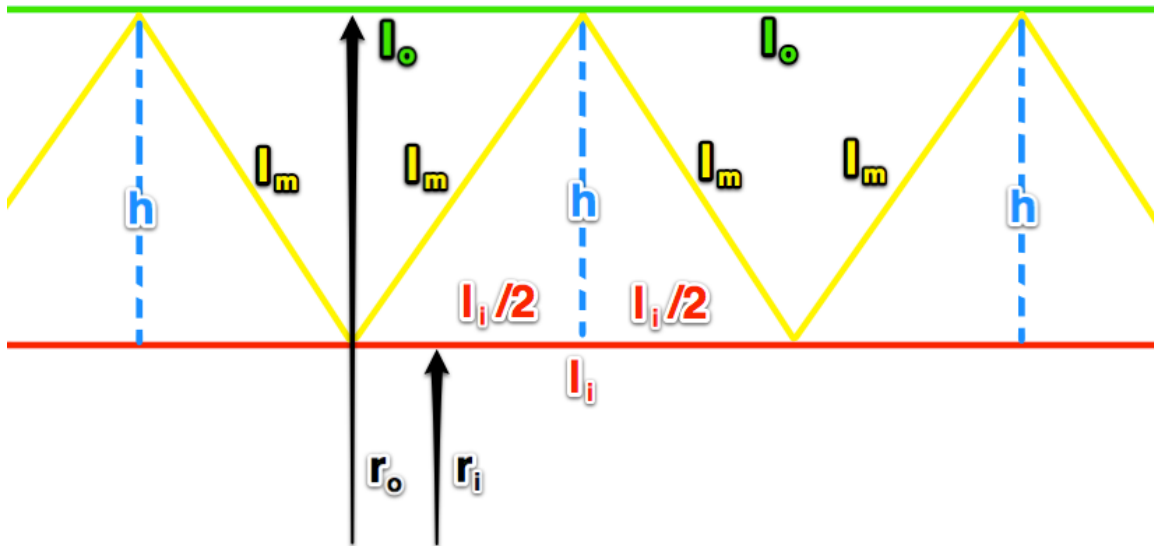


[Figure 3.7] Boundary truss triangles that has been straightened out

If the circular boundary truss is straightened out and the inner triangles are roughly equilateral so that $l_i \approx l_m$ as shown in [Figure 3.7], h is given by [Equation 3.24].

$$h = \sqrt{l_m^2 - \frac{l_i^2}{2^2}} = \sqrt{\left(\frac{2\pi}{4m} r_i\right)^2 - \frac{1}{4} \left(\frac{2\pi}{4m} r_i\right)^2} = \frac{\pi\sqrt{3}}{4m} r_i$$

[Equation 3.24]

Substituting in [Equation 3.24], the ratio between r_i and r_o is given by [Equation 3.25] which is vital for determining the geometry of the frame.

$$\frac{r_o}{r_i} = \frac{r_i + h}{r_i} = \frac{1}{r_i} \left(r_i + \frac{\pi\sqrt{3}}{4m} r_i \right) = 1 + \frac{\pi\sqrt{3}}{4m}$$

[Equation 3.25]

3.4 Dynamic Relaxation Algorithm

The method of dynamic relaxation algorithm is adapted from Alistair Day's dynamic relaxation technique, which uses simplified version of the Verlet algorithm (Day, 1965). The forces in the nodes are carried over in the next iteration with some damping to accelerate the number of steps required to reach static equilibrium (Williams, n.d.). The algorithm is briefly outlined by [Figure 3.8], and repeated until static equilibrium is attained.

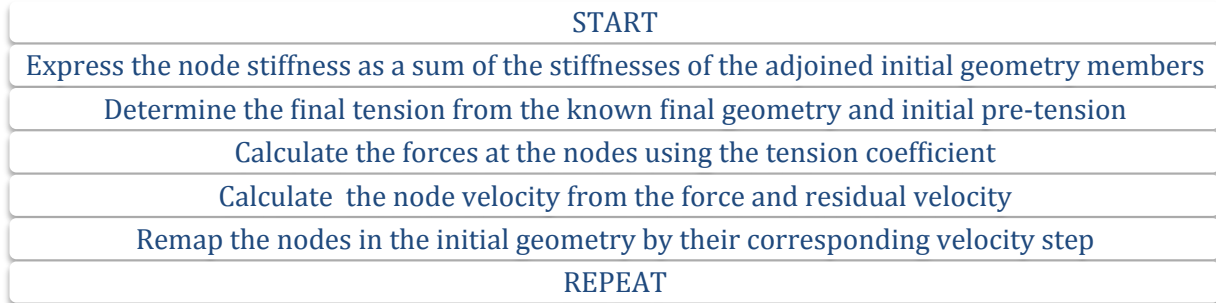


[Figure 3.8] Dynamic Relaxation Algorithm

3.4.1 From Strained to Unstrained Geometry

The London Olympic Stadium [Figure 3.9] inspires the concept of a perimeter that is free to expand outwards or contract inwards independent of the rest of the structure. This contrasts with the Olympic Velodrome, a denser grid of stiff truss formation that resists horizontal movement. Investigation of the potential benefits of isolating the loads is beyond the scope of this investigation. However, if the perimeter is free to move, the question naturally arises as to what the initial unstrained shape has to be if the shape of the strained final geometry is the known, desired geometry. The dynamic modification algorithm was modified to solve this problem.



[Figure 3.9] London Olympic Stadium (Left) and London Olympic Velodrome (Right)

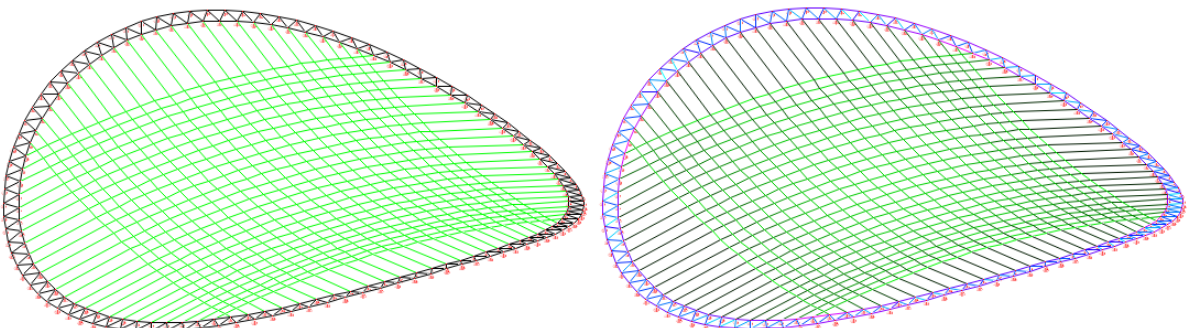


[Figure 3.10] Pre-strained (unknown geometry) vs. defined final geometry (unknown stress)

In the analyses that performed in [Section 5], the modified dynamic relaxation algorithm determines the unstrained initial geometry. The effective tension is determined from the known strained geometry and initial pretension as outlined in [Table 3.1].

	Notation	State
Length of the unstrained members	L'_k	Unknown
Length of the strained members	L_k	Known
Pretension in the cables	T'_k	Known
Final tension in the cables	T_k	Unknown

[Table 3.1] Known and unknown variables

3.4.2 Stiffness of the nodes

The node stiffness K_i is the sum of the elastic stiffness of the initial geometry members connecting to the node expressed as [Equation 3.26], refreshed at every iteration.

$$K_i = \sum \frac{EA_k}{L'_k} \text{ where } i = \{1 \dots \text{Last Node}\}, k = \{\text{Members connected to Node } i\}$$

[Equation 3.26]

3.4.3 Tension Coefficient

For a given member k , the relationship between stress σ_k , strain ε_k and young's modulus E_k are well known, described by [Equation 3.27]. The stress σ_k , is also axial force T_k over member cross-sectional area A_k [Equation 3.28].

$$\sigma_k = E_k \cdot \varepsilon_k$$

[Equation 3.27]

$$\sigma_k = \frac{T_k}{A_k}$$

[Equation 3.28]

For small strain values where $L_k \approx L'_k$ where L_k being the strained length and L'_k the unstrained length, the following relationship for strain can be derived using the Finite Strain Theory in Continuum Mechanics (Dill, 2007),

$$\varepsilon_k = \frac{1}{2} \frac{L_k^2 - L'^2_k}{L'^2_k} = \frac{1}{2} \frac{(L_k + L'_k)(L_k - L'_k)}{L'^2_k} = \frac{2}{2} \frac{L'(L_k - L'_k)}{L'^2_k} = \frac{L_k - L'_k}{L'_k}$$

[Equation 3.29]

If T'_k is the known pretension and T_k is the unknown effective tension, substituting [Equation 3.28] and [Equation 3.29] into [Equation 3.23],

$$\begin{aligned} \frac{T_k - T'_k}{A_k} &= \frac{E_k(L_k - L'_k) - E_k(L'_k - L'_k)}{L'_k} \\ T_k &= T'_k + \frac{EA_k(L_k - L'_k)}{L'_k} \end{aligned}$$

[Equation 3.30]

3.4.4 Forces at the nodes

For the geometry to be in static equilibrium, the sum of forces at any given constituent node must equate to zero. This is described by [Equation 3.31]. The force is calculated for each member as a product of its resultant length $\delta L'_{kj}$ in the direction of force and tension coefficient $\frac{T_k}{L'_k}$, which is the final tension per unit initial length.

$$F_{ij} = \sum \frac{T_k}{L'_k} (X'_{(End_{k, this}), j} - X'_{(End_{k, that}), j}) \rightarrow 0$$

where $i = \{1 \dots \text{Last Node}\}, j = \{x, y, z\}, k = \{\text{Members connected to Node } i\}$

[Equation 3.31]

3.4.5 Determining node velocity

Until static equilibrium, the nodes move at a velocity determined by the force acting on the node, onto which velocity from the previous time step t is also lumped with some damping c . It is described by [Equation 3.32] where index i corresponds to the node number and j corresponds to the direction of velocity.

$$v_{ij}^{t+dt} = c \cdot v_{ij}^t + \frac{F_{ij}}{K_i} \rightarrow 0 \text{ where } i = \{1 \dots \text{Last Node}\}, j = \{x, y, z\}$$

[Equation 3.32]

3.4.6 Remapping the initial geometry

Each velocity step is added to the record of initial co-ordinates to remap the state of the initial geometry as described by [Equation 3.33]. Then the entire process is repeated until static equilibrium.

$$X'_{ij} = X'_{ij} + v_{ij}^{t+dt} \text{ where } i = \{1 \dots \text{Last Node}\}, j = \{x, y, z\}$$

[Equation 3.33]

3.5 Sliding of cables

To allow sliding of cables means all the members that make up a continuous cable experiences the same amount of strain as the total strain for the entire length of cable. This is to enable comparison in [Section 5] to determine how slide influences the frame stiffness as opposed to when the cables are restrained at nodes. The strain for the entire length of a given cable is calculated and the same strain value is assigned to each individual member that the cable constitutes. As the tension is uniform in the given cable, [Equation 3.30] is re-examined in [Equation 3.34] where k corresponds to each individual member of a given continuous cable.

$$\delta T_{cable} = T_{cable} - T'_{cable} = EA_{cable} \frac{\sum L_k - \sum L'_k}{\sum L'_k}$$

[Equation 3.34]

If the initial tension T'_{cable} is predefined and assumed constant throughout the cable as shown in [Figure 3.11], and the effective tension T_{cable} is not predefined but also constant due to the opportunity to slide, [Equation 3.35] can be derived if EA_{cable} is also assumed to remain constant.

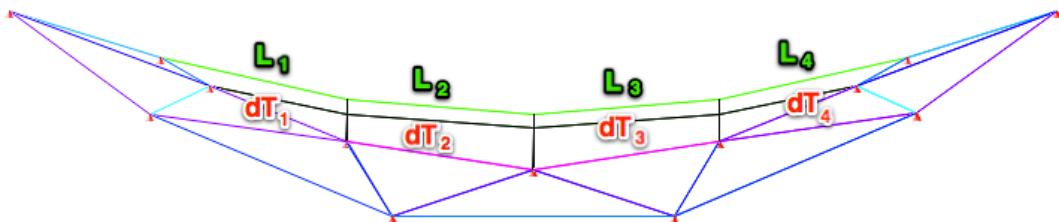


[Figure 3.11] Elevation of continuous cable members where $m = 3$

$$\frac{\delta T_{cable}}{EA_{cable}} = \frac{\sum L_k - \sum L'_k}{\sum L'_k} = \frac{T_k - T'_k}{EA_k} = \frac{L_k - L'_k}{L'_k} = constant$$

[Equation 3.35]

For each of the individual member of a given cable, the relationship between the strained length L_k and the unstrained length L'_k is given by [Equation 3.36] if $\frac{\delta T_{cable}}{EA_{cable}}$ is a constant.

$$L_k = L'_k + L'_k \frac{\delta T_{cable}}{EA_{cable}}$$

[Equation 3.36]

$$L'_k = \frac{L_k}{1 + \frac{\delta T_{cable}}{EA_{cable}}}$$

[Equation 3.37]

3.6 Cable pre-strain and resultant frame axial strain

The cable pre-strain $\varepsilon_{i,cables}$ is described by [Equation 3.38] where index $i = \{x, y\}$ is the DOF, $T'_{i,cables}$ is the sum of total pre-stress force applied as shown in [Figure 3.12] and $EA_{i,cable}$ is the sum of cable EA in DOF indicated by i . The axial strain of the frame $\varepsilon_{i,frame}$ is given by [Equation 3.39] where $L_{i,frame}$ is the strained span and $L'_{i,frame}$ is the unstrained span of the frame along the major axes.

The ratio of $\varepsilon_{i,cables}$ and $\varepsilon_{i,frame}$, described by S_i [Equation 3.40], is the non-dimensional indication of frame stiffness. It describes how the amount of pre-strain in the cables affects the amount of axial strain experienced by the frame along each DOF.

An equal amount of pre-strain is applied in the cables along each DOF such that $\varepsilon_{x,cables} = \varepsilon_{y,cables}$. As the aspect ratio of the frame $a_x : a_y = 1:1$ and as there are no imposed loads acting on the model for any of the tests, as the sole effect of pre-strain is being examined $\varepsilon_{x,frame} = \varepsilon_{y,frame}$. Therefore, the ratios $S_x = S_y$ are also equal.

$$\varepsilon_{i,cables} = \frac{T'_{i,cables}}{EA_{i,cable}}$$

[Equation 3.38]

$$\varepsilon_{i,frame} = 1 - \frac{L_{i,frame}}{L'_{i,frame}}$$

[Equation 3.39]

$$S_i = \frac{\varepsilon_{i,cables}}{\varepsilon_{i,frame}}$$

[Equation 3.40]

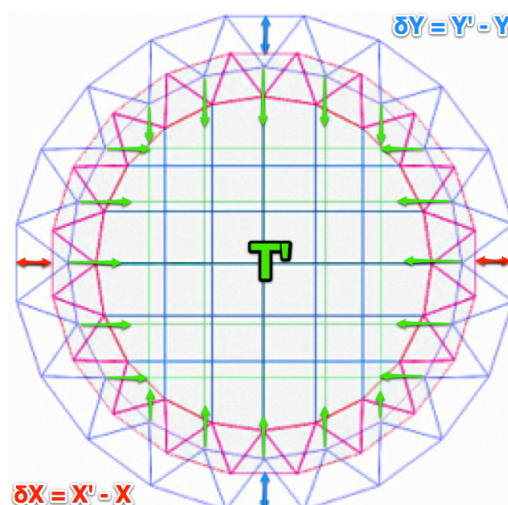


[Figure 3.12] Plan view of frame deformation due to pre-strain

4 Common Assumptions and Definitions

4.1 Material

As the cables would buckle if subjected to any compressive force, they are assumed to lack compressive strength. Cable pre-strain is intended to resist this compressive action. The buckling effect of the truss is ignored as trusses with different thicknesses would have different limits therefore has to be assessed separately. The boundary truss and the cables are steel members with properties listed in [Table 4.1] for the intents and purposes of the discussion.

Property	Notation	Truss	Cables
Young's Modulus	E	200 GPa	200000 GPa
Tensile Strength	f_t	500 MPa	500 MPa
Compressive Strength	f_c	500 MPa	0 MPa
Strain Limit	ϵ	0.2%	0.2%

[Table 4.1] Material properties

4.2 Reference Frame

The attributes in [Table 4.2] characterises the reference frame visible in [Figure 4.1]. Unless otherwise stated, it will be used throughout the tests described in [Section 5].

Property	Notation	Value
Number of Cables per Axis	m	25
Truss Radius	r_{truss}	40 mm
Truss Thickness	t_{truss}	10 mm
Inner Truss Length	l_i	2500 mm
Cable Radius	r_{cable}	10 mm
Frame Outer Radius	r_o	41.9 m
Cross sectional area ratio	$A_{truss}:A_{cable}$	7.0
Frame Aspect Ratio	$a_x:a_y$	1:1
Frame Curvature Ratio	$b_x:b_y:b_z$	1:1:0.15

[Table 4.2] Properties of the frame to be used as a reference frame

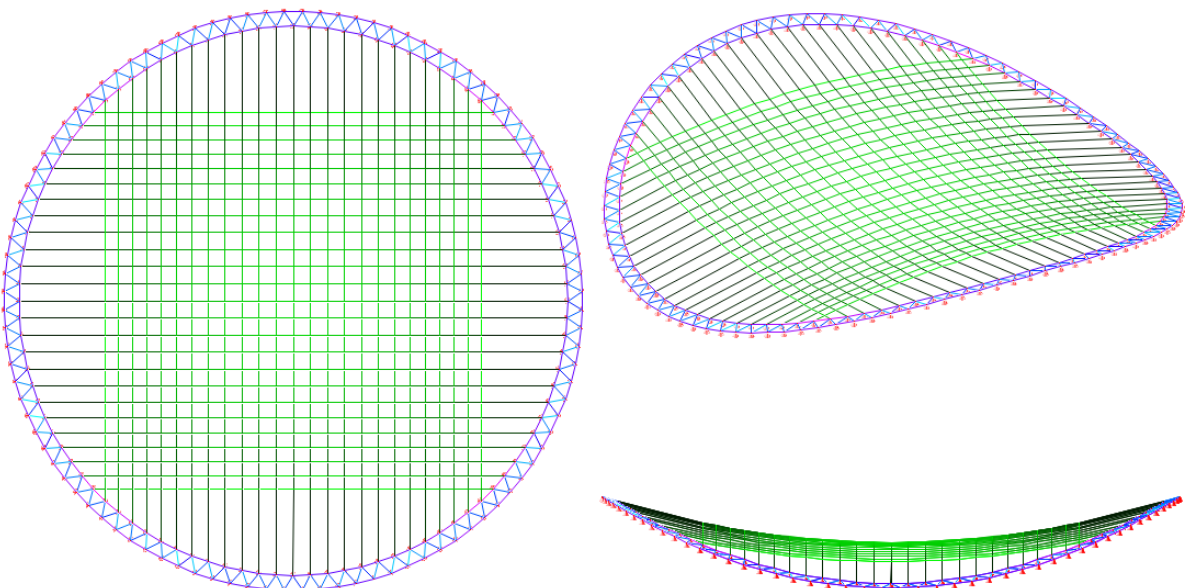


[Figure 4.1] Anticlockwise: Plan, elevation and isometric view of the reference frame

5 Results and Discussions

5.1 Test 1: Axial strain due to cable pre-strain and truss to cable x-sectional ratio

5.1.1 Aim of the test

The primary aim of the test will be to determine how $\varepsilon_{i,frame}$ changes due to $\varepsilon_{i,cables}$ when the ratios of the cross sectional areas of boundary truss to the cables, $A_{truss}:A_{cable}$ changes. The secondary aim of this test will be to establish the difference in this behaviour when the cables are restrained at the nodes (shortened to non-slide) as opposed to when they are allowed to slide.

5.1.2 Procedure

For this test, the $\varepsilon_{i,cables}$ is incremented slowly until the amount of stress experienced by any given individual member surpasses its strength limit described in [Table 4.1]. Other properties of the frame are identical to that of the reference frame defined in [Table 4.2].

The $A_{truss}:A_{cable}$ ratios given in [Table 5.1] are the variables. The $A_{truss}:A_{cable}$ ratio is influenced by A_{truss} since A_{cable} is constant. In total, 8 tests, each corresponding to different $A_{truss}:A_{cable}$ ratios are conducted for the non-slide case and then repeated for the slide case to establish the extent to which this affects the behaviour.

t_{truss} (mm)	16	14	12	10*	8	6	4	2
A_{truss} (mm ²)	3217	2903	2564	2199	1809	1394	955	490
A_{cable} (mm ²)	314	314	314	314	314	314	314	314
$A_{truss}:A_{cable}$	10.2	9.2	8.2	7.0	5.8	4.4	3.0	1.6

[Table 5.1] Table of x-sectional area ratio variables tested (*Reference frame)

5.1.3 Results and Discussion

[Figure 5.1] and [Figure 5.2] show the correlation between $\varepsilon_{i,cables}$ (T'/EA) and $\varepsilon_{i,frame}$ (δ/L') experienced by the frame for non-slide and slide case respectively. The gradient of $\varepsilon_{i,cables}$ to $\varepsilon_{i,frame}$ is the non-dimensional indication of stiffness S_i ($(T'/EA)/(\delta/L')$) along the major axes. It can be observed that with increasing $A_{truss}:A_{cable}$ ratio, S_i increases, as the frame experiences reduction in $\varepsilon_{i,frame}$. This suggests that the boundary truss plays a significant role in the stiffness of the frame.

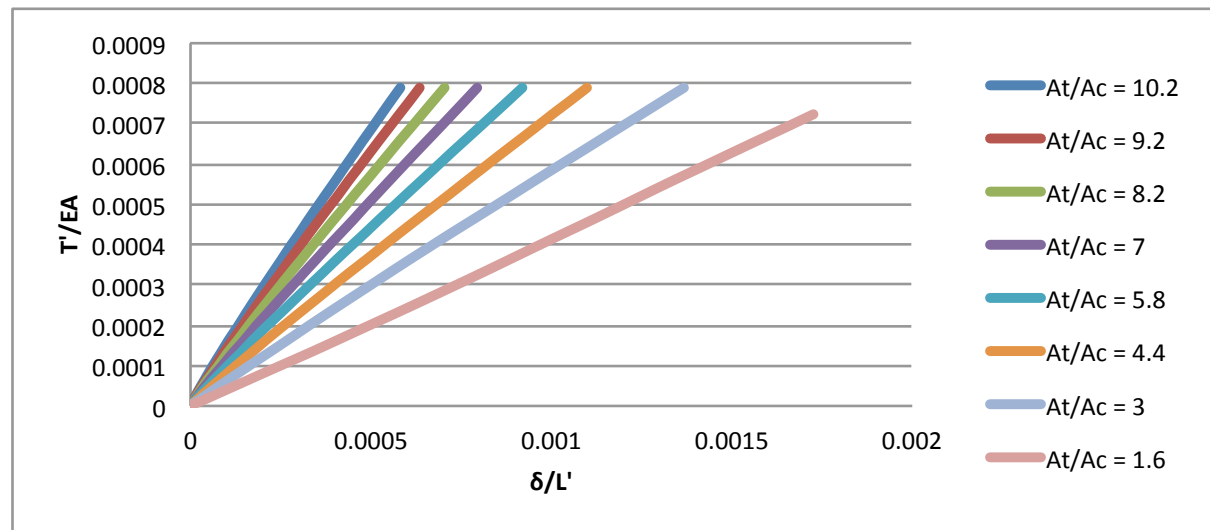


[Figure 5.1] Cable pre-strain (T'/EA) vs. axial strain (δ/L') for various $A_{truss}:A_{cable}$ ratio (Non-slide)

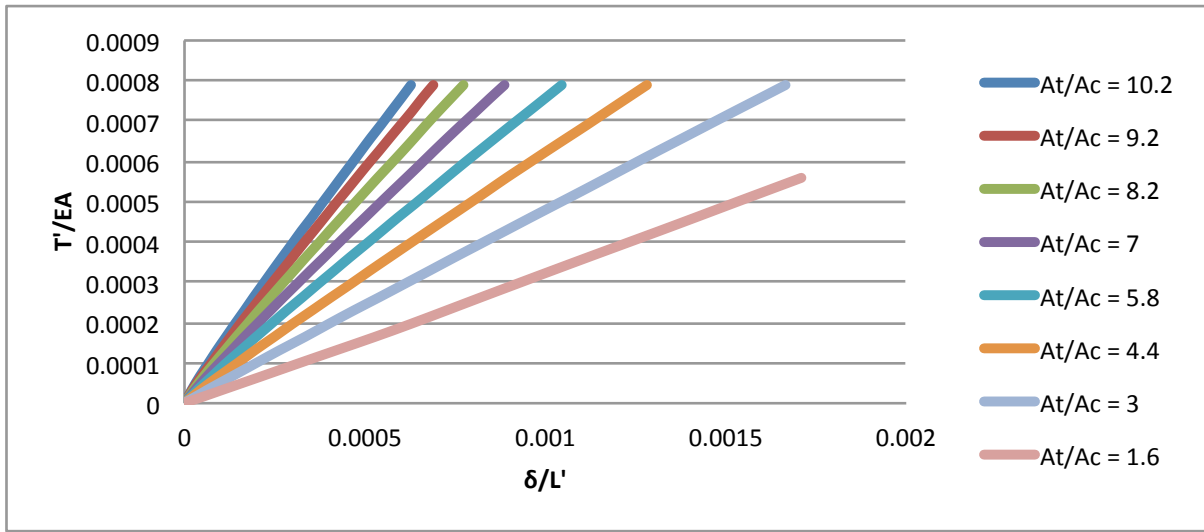


[Figure 5.2] Cable pre-strain (T'/EA) vs. axial strain (δ/L') for various Atruss:Acable ratio (Slide)

With decreasing $A_{truss}:A_{cable}$, S_i decreases as the frame experiences increase in $\varepsilon_{i,frame}$. But the trends also show for $A_{truss}:A_{cable} \approx 1.6$ that there is reduction in the amount of $\varepsilon_{i,cables}$ that can be applied. As most of the $A_{truss}:A_{cable}$ ratios fail due to limit imposed by cable cross sectional capacity for both non-slide and slide cases, this suggests that the capacity of the truss and cable cross-section to resist $\varepsilon_{i,cables}$ varies with change in $A_{truss}:A_{cable}$ ratio. The $A_{truss}:A_{cable} \approx 1.6$ fails due to limit imposed by truss cross sectional capacity. Higher $A_{truss}:A_{cable}$ ratio can be expected to fail due to limit imposed by cable cross-sectional stress capacity and lower $A_{truss}:A_{cable}$ ratios due to limit imposed by truss cross-sectional stress capacity. The benefit of increasing the truss cross-sectional area to stiffen the structural frame becomes void as the cable cross sectional capacity increasingly governs the failure limit.

There is an optimum $A_{truss}:A_{cable}$ ratio where the full cross-sectional capacity of truss and cables are mobilised using the least amount of material while providing the highest stiffness possible. For the non-slide case, $A_{truss}:A_{cable} \approx 3.0$ approximates the optimum as it allows for the highest $\varepsilon_{i,cables}$ for the lowest $A_{truss}:A_{cable}$ ratio. Increasing $A_{truss}:A_{cable}$ ratio and $\varepsilon_{i,cables}$ slowly would give a higher degree of accuracy.

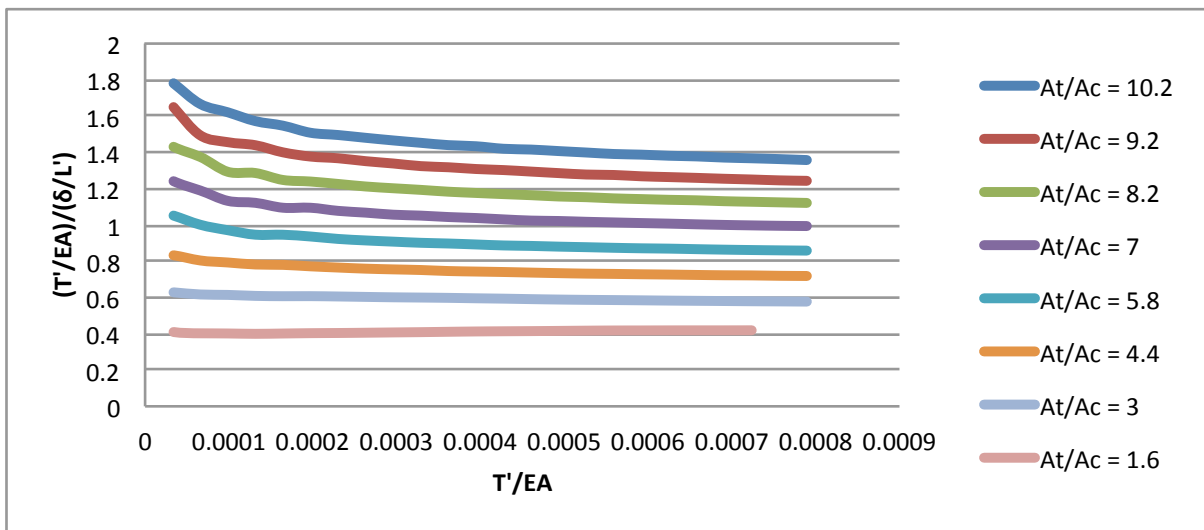


[Figure 5.3] Si $((T'/EA)/(δ/L'))$ vs. cable pre-strain (T'/EA) for various Atruss:Acable ratio (Non-slide)

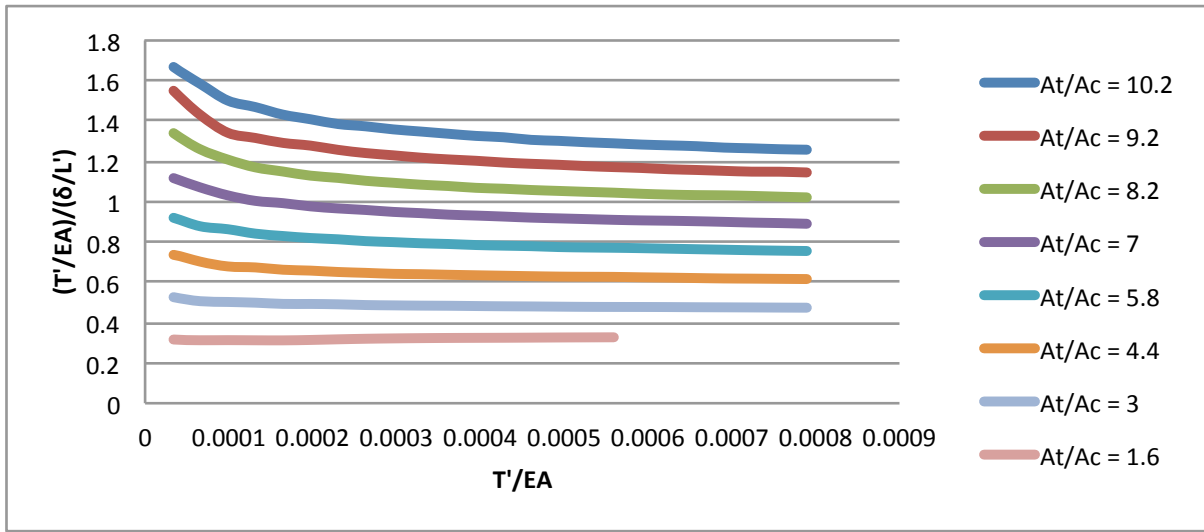


[Figure 5.4] Si $((T'/EA)/(\delta/L'))$ vs. cable pre-strain (T'/EA) for various Atruss:Acable ratio (Slide)

[Figure 5.3] and [Figure 5.4] demonstrate that, with increasing $\varepsilon_{i,cables}$, there is reduction in S_i . This trend is observable in almost all cases of $A_{truss}:A_{cable}$. The exception when $A_{truss}:A_{cable} \approx 1.6$ for both slide and non-slide cases are due to the inability of the cross-sectional area of the truss to carry the experienced stresses causing premature failure. The general reduction of S_i however, may be attributed to deformation mechanisms that aid to increase $\varepsilon_{i,frame}$ frame due to increasing $\varepsilon_{i,cables}$.

When the $A_{truss}:A_{cable} \approx 7.0$ and $A_{truss}:A_{cable} \approx 8.2$ for non-slide and slide cases respectively, the minimum $S_i \approx 1.0$ when $\varepsilon_{i,cables} > 0.0007$ where the rate at which the cables experience strain is similar to the rate at which the frame experience axial strain as $\varepsilon_{i,cables} \approx \varepsilon_{i,frame}$.

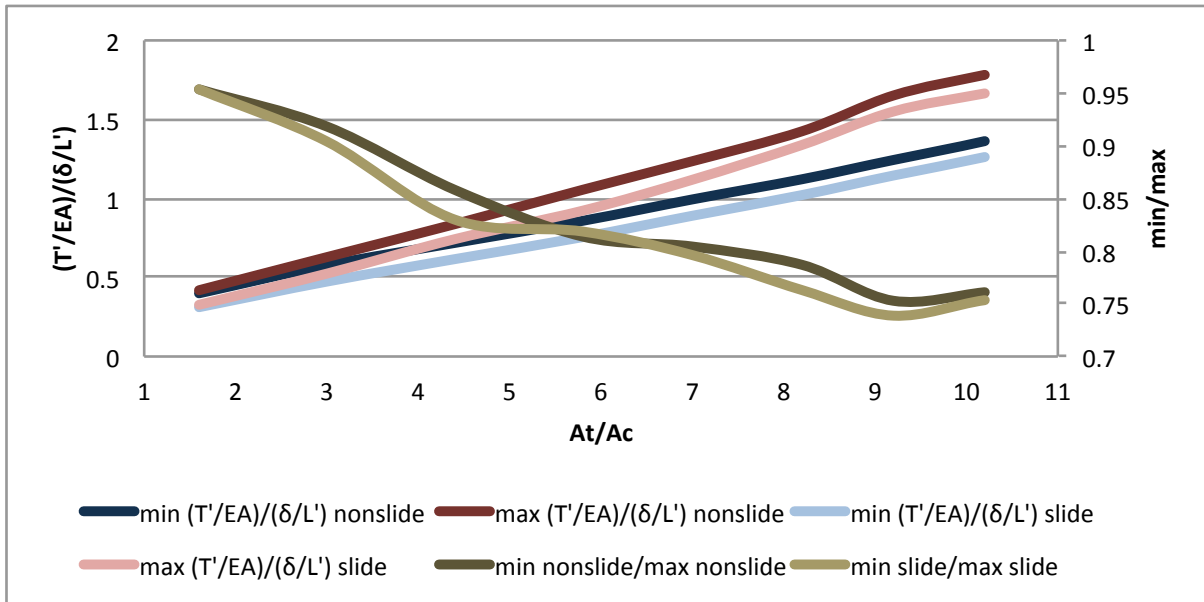


[Figure 5.5] Si $((T'/EA)/(\delta/L'))$ ratio vs. Atruss:Acable ratio

To continue the discussion, [Figure 5.5] shows the correlation between maximum and minimum S_i against their corresponding $A_{truss}:A_{cable}$ ratio for slide and non-slide cases. The graph confirms that there is a positive linear correlation between S_i and $A_{truss}:A_{cable}$ for both slide and non-slide cases.

The ratio of the minimum and maximum S_i for both slide and non-slide cases show that, minimum $S_i \approx 75\%$ of maximum S_i for the highest $A_{truss}:A_{cable} \approx 10.2$ tested within the range of variables. This contrasts with just around 95% for the lowest $A_{truss}:A_{cable} \approx 1.6$. This reveals that the discrepancy between the two values is greater when $A_{truss}:A_{cable}$ is higher for both slide and non-slide cases.

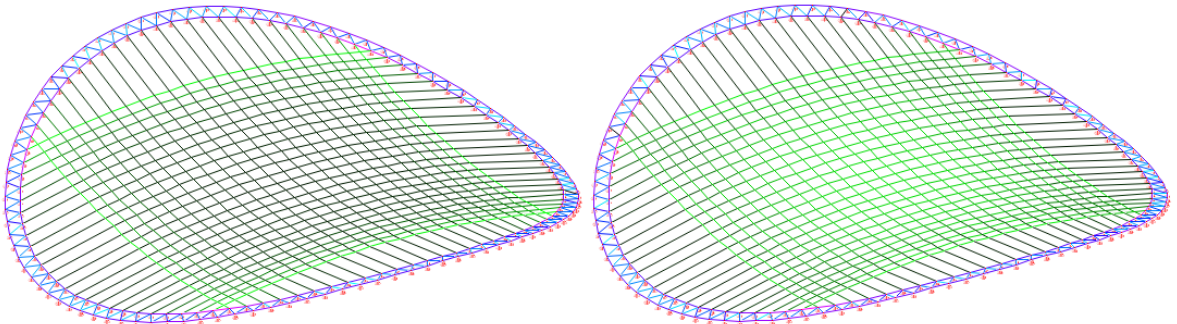


[Figure 5.6] Slide (Left) vs. non-slide (Right) m=25 where (Max stress=Green, Min stress=Black)

[Figure 5.5] also shows that, when maximum and minimum slide S_i are compared against maximum and minimum non-slide S_i , both maximum and minimum non-slide S_i are greater than slide S_i . When cables are allowed to slide, strain is concentrated on edge cable strands as observable in [Figure 5.6]. When they are restrained, there is greater uniformity in the final stress distribution with smaller difference in the maximum and minimum final stress distribution. As a consequence, a greater $A_{truss}:A_{cable}$ ratio is required to achieve the same axial stiffness, which is not efficient.

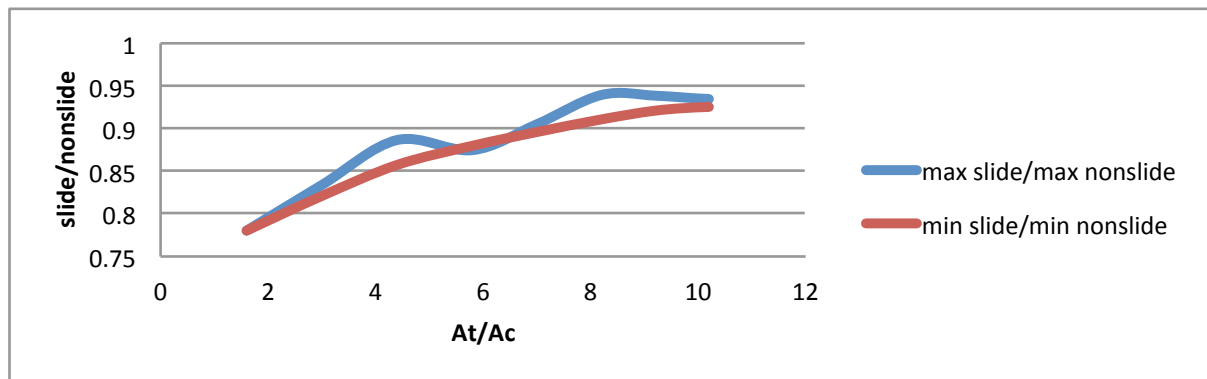


[Figure 5.7] Maximum and minimum slide S_i /non-slide S_i vs. $A_{truss}:A_{cable}$ ratio

[Figure 5.7] shows the ratio of the maximum slide S_i to non-slide S_i and the ratio of minimum slide S_i to non-slide S_i . The trend is slightly unstable for the ratio of the maximum S_i but follows a similar positive trend to the ratio of the minimum S_i . The ratio of slide to non-slide S_i tends towards 1 as $A_{truss}:A_{cable}$ increases. This confirms smaller discrepancy between the values when $A_{truss}:A_{cable}$ is high. Also, the minimum S_i is best assumed to be the effective S_i as it is the lowest value.

5.1.4 Limitations

The buckling failure of the truss due to slenderness as $A_{truss}:A_{cable}$ ratio varies have not been accounted for in these analyses. The effect of this on the actual behaviour of the frame may be significant. The frictional forces resisting the cable slide have not been accounted for either, which in reality, would influence the actual distribution of stresses.

5.2 Test 2: Axial strain due to cable pre-strain and the number of cables

5.2.1 Aim of the test

This test aims to establish how the influence of pre-strain varies as the number of cables per quarter per DOF, m , varies in each direction. The second part of this test aims to examine the effect of cable slide and its influence on the stiffness of the structural frame as m varies.

5.2.2 Procedure

For this test, number of cables per quarter per DOF, m tabulated in [Table 5.2] are examined. This affects the strained radius of the inner ring and the outer ring shown in [Figure 3.3] in the pattern illustrated in [Figure 5.8]. In total, there are 7 tests corresponding to each m . These 7 tests are initially conducted for the non-slide case and then repeated for the slide to understand the difference.

For bigger values of m , ratio of the outer to inner radius $r_o:r_i$ is smaller to meet the geometrical constraint of maintaining the roughly equilateral inner triangles in the boundary truss. A similar magnitude of $\varepsilon_{i,cables}$ is applied despite the varying $r_o:r_i$ ratio and increasing m . Other properties of the frame are identical to that of the reference frame defined in [Table 4.2].

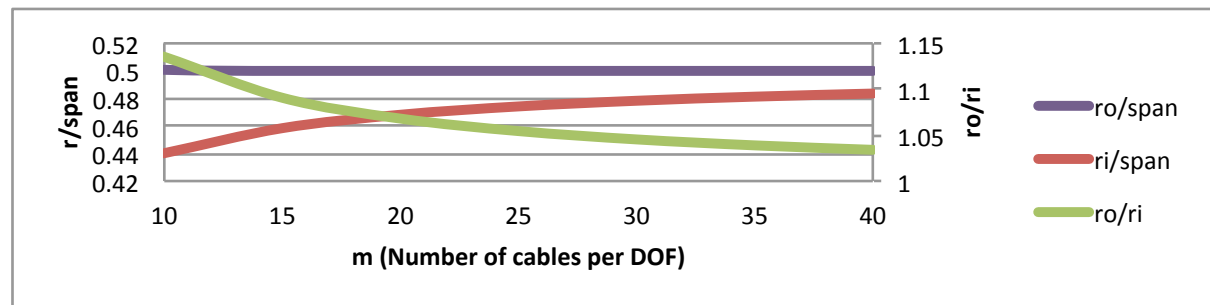


[Figure 5.8] Radius and radial ratio vs. m (Number of cables per direction)

m	10	15	20	25*	30	35	40
r_o / span	0.5	0.5	0.5	0.5	0.5	0.5	0.5
r_i / span	15.9	23.8	31.8	39.8	47.7	55.7	63.7
$r_o : r_i$	114%	109%	107%	105%	105%	104%	103%

[Table 5.2] Change in outer radius with the change in number of cables (*Reference frame)

5.2.3 Result and Discussion

In [Figure 5.9] and [Figure 5.10], with increasing m , the gradient $S_i ((T'/EA)/(\delta/L'))$ becomes steeper due to increasing $\varepsilon_{i,cables}$ (T'/EA) and decreasing $\varepsilon_{i,frame}$ (δ/L') for both slide and non-slide cases. This could be attributed to increasing number of cable intersections and number of connections to the boundary nodes leading to greater uniformity in force transfer from the cables to the boundary truss. For the slide case S_i for $m \approx 15$ is steeper than the S_i for $m \approx 10$ but the configuration still manages to retain a greater $\varepsilon_{i,cables}$ capacity. The cause of this anomaly may require a closer inspection.

When S_i is plotted against $\varepsilon_{i,cables}$ for non-slide case in [Figure 5.11] and for slide case in [Figure 5.12], both show a reduction in S_i as $\varepsilon_{i,cables}$ increases. When $\varepsilon_{i,cables} \approx \varepsilon_{i,frame}$ so that $S_i \approx 1.0$, $m \approx 25$ for the non-slide case and $m \approx 30$ for the slide case. 5 additional cables would be required in this case to achieve the same level of stiffness as the non-slide case if the cables were allowed to slide.

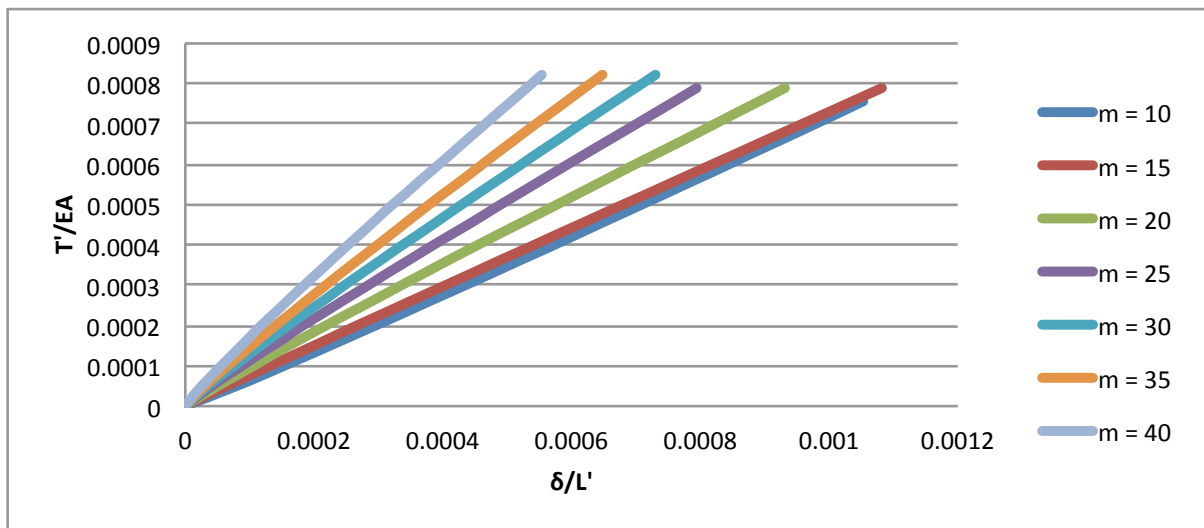


[Figure 5.9] Cable pre-strain (T'/EA) vs. axial strain (δ/L') for various m (Non-slide)

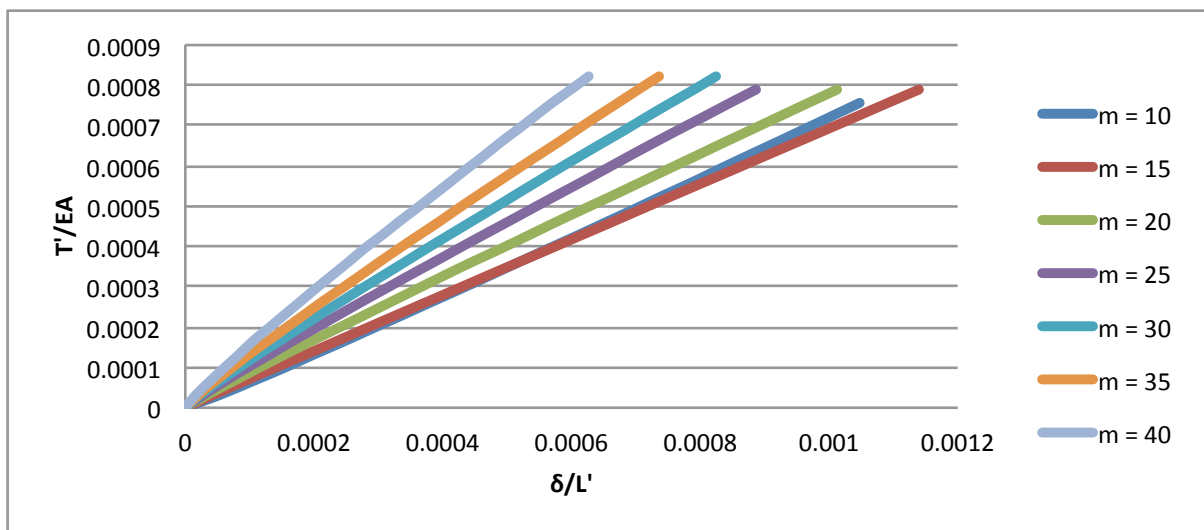


[Figure 5.10] Cable pre-strain (T'/EA) vs. axial strain (δ/L') for various m (Slide)

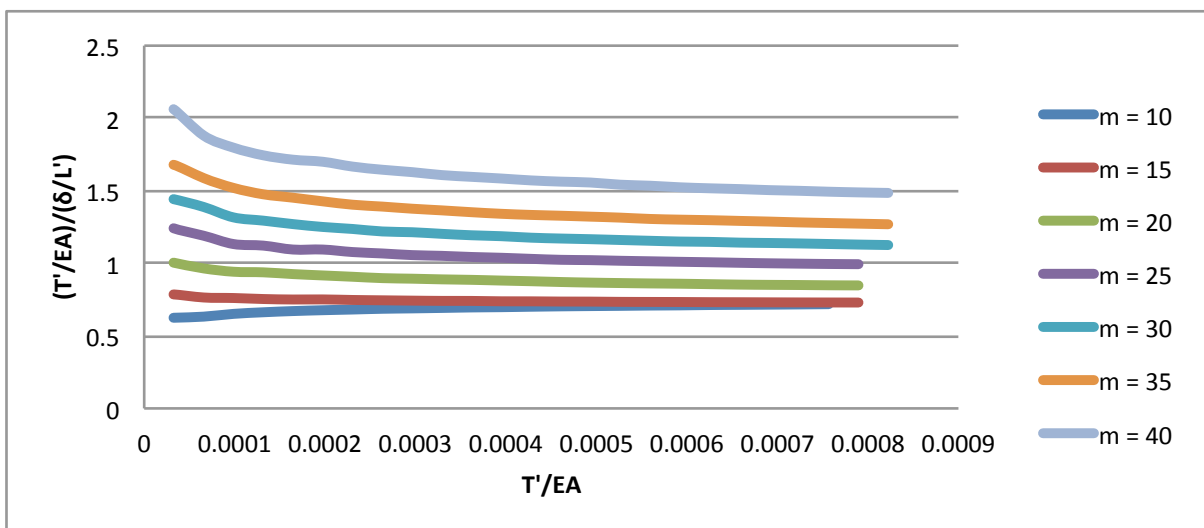


[Figure 5.11] Si ($(T'/EA)/ (\delta/L')$) ratio vs. cable pre-strain (T'/EA) for various m (Non-slide)

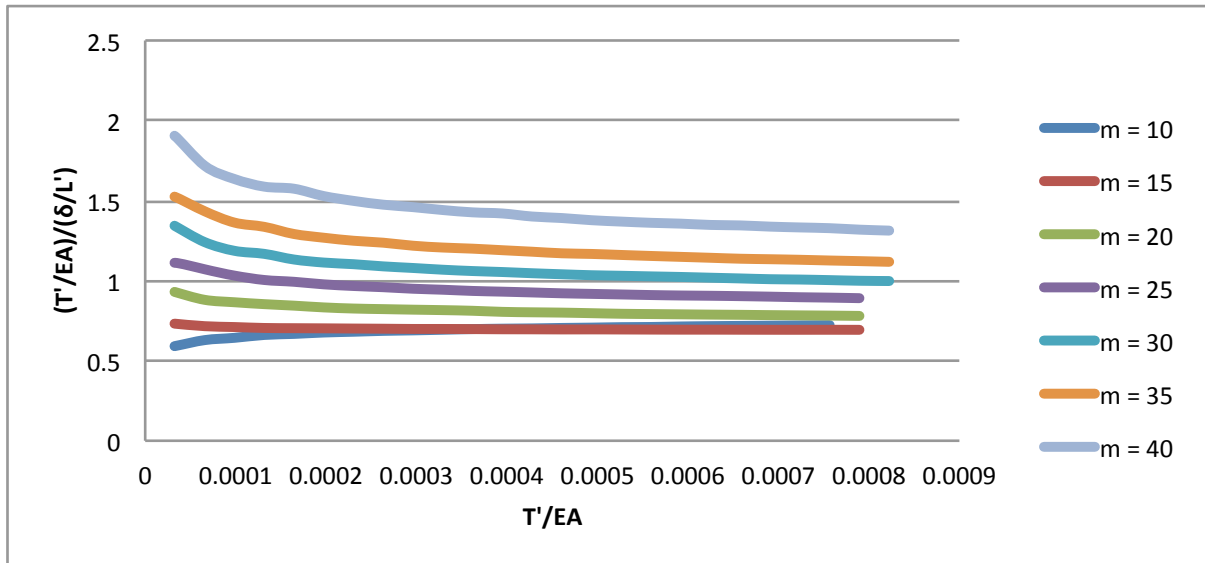


[Figure 5.12] Si $((T'/EA)/(\delta/L'))$ ratio vs. cable pre-strain (T'/EA) for various m (Slide)

In [Figure 5.13], the ratios of the maximum and minimum S_i show increasing discrepancy for m greater or smaller than 15 for both slide and non-slide case. The mechanisms that cause these discrepancies seem dependent either on m or $r_o:r_i$ as they are the only changing variables.

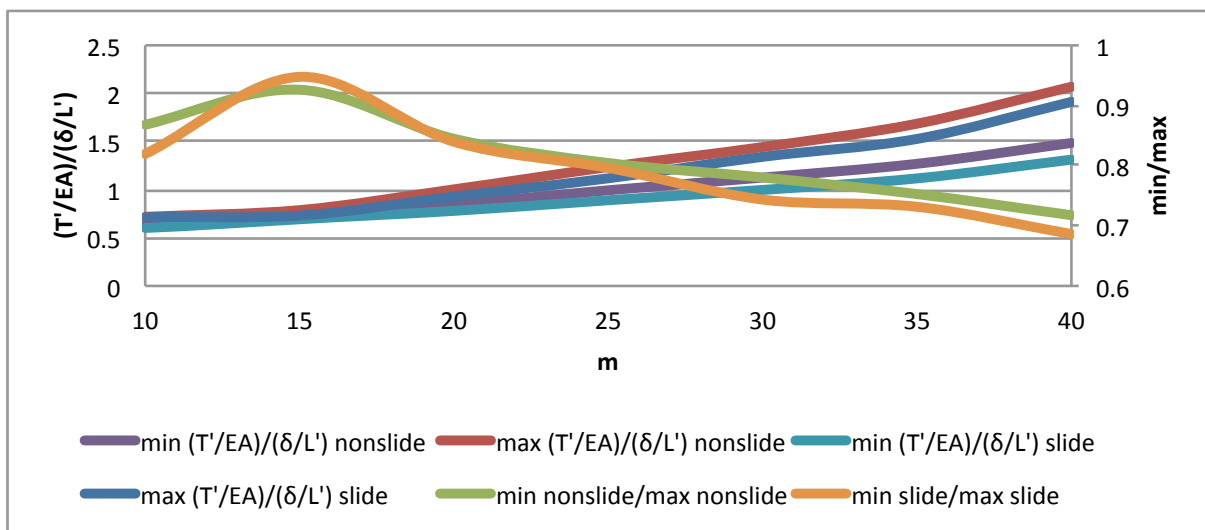


[Figure 5.13] Si $((T'/EA)/(\delta/L'))$ ratio vs. m

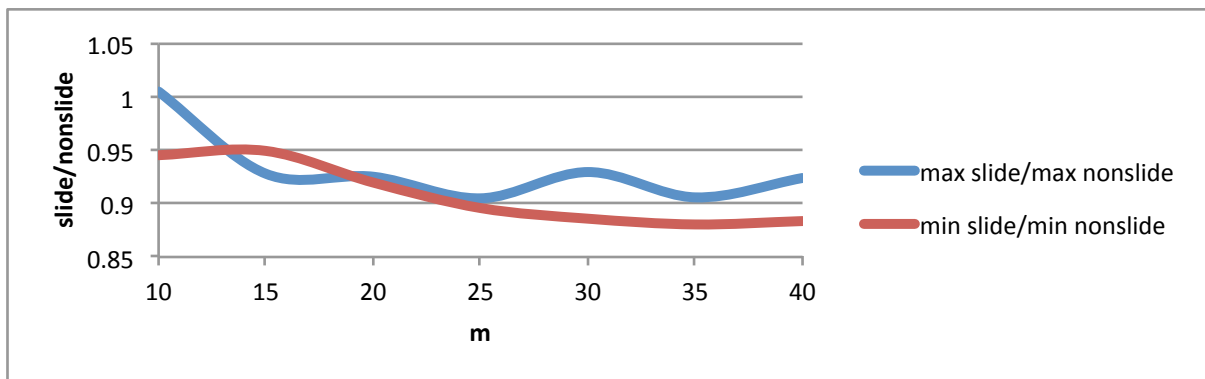


[Figure 5.14] Maximum and minimum slide Si/non-slide Si vs. m

[Figure 5.14] plots the ratios of maximum slide S_i to non-slide S_i and minimum slide S_i to non-slide S_i against m . While the ratios of the maximum have a slightly irregular trend, there is greater the discrepancy in both cases as m increases, demonstrating that cable slide has lesser influence on the frame stiffness when there are fewer cables.

5.2.4 Limitations

These results of from these tests are applicable within the defined range. Whether the deductions can be generalised to frames with other aspect ratios or arrangement of cable-net layout still needs to be determined.

5.3 Test 3: Axial strain due to special case of cable arrangement

5.3.1 Aim of the test

The test aims to compare a special case of cable arrangement with an ordinary form of cable arrangement with identical values of m but different number of cables per DOF. The test also aims to establish the differences in the cable arrangements with identical number of cables per DOF but varying m .

5.3.2 Procedure

The special case of cable arrangement has cables spanning from all the nodes in one half of the boundary truss to the other half in both DOF. Unlike m , which is the number of cables per quarter per DOF applicable to the ordinary form of cable arrangement, m^* is the number of cables per half per DOF, which equates to the number of cables for the special case of cable arrangement, as listed in [Table 5.3]. In total, there are 7 tests corresponding to each m . These 7 tests are initially conducted for the non-slide case and results for ordinary non-slide case are borrowed from [Test 2] to distinguish the difference.

[Figure 5.15] shows a growing trend for the amount of cable material required per unit span with increasing m for both cases of cable arrangement. However, the special case demands 41% more cable material than the ordinary case. The differences that additional cables make to the frame stiffness are measured to understand which form gives a more efficient outcome. As it is clear that it serves as a better decision to restrain the cables, all the tests are conducted for non-slide case. Other properties of the frame are identical to the reference frame defined in [Table 4.2]. The results will also be used to compare differences between frames where $m = m^*$ to see which of the two is stiffer.

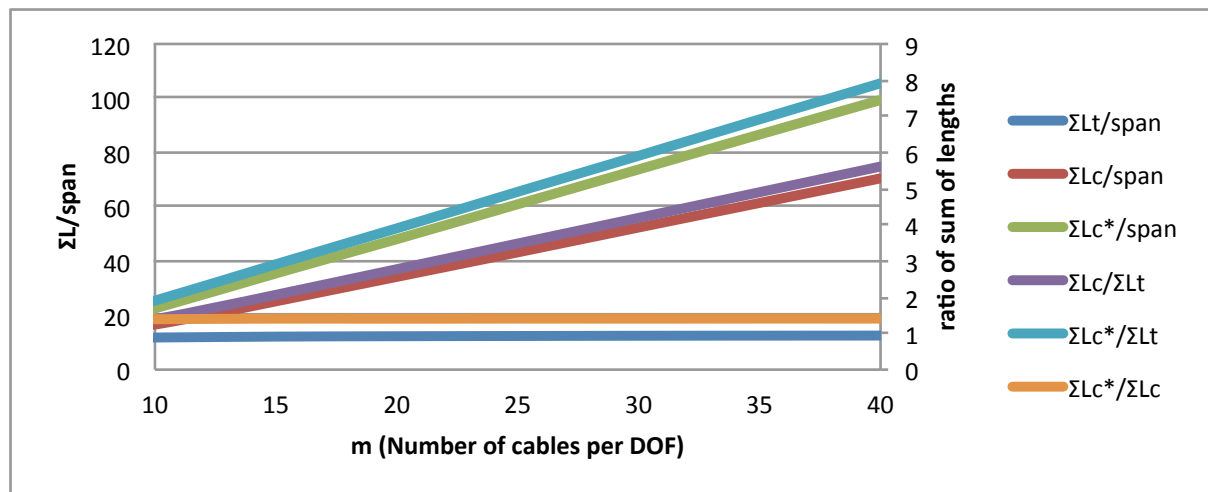


[Figure 5.15] Number of cables vs. the total length of truss and cables and their ratios

m	10	15	20	25*	30	35	40
$m^&$	18	29	38	49	58	69	78
$\Sigma L_{truss}/span$	23.65	24.34	24.62	24.80	24.97	25.05	25.11
$\Sigma L_{cable}/span$	32.15	50.31	68.35	86.43	104.74	122.84	140.95
$\Sigma L_{cable}^&/span$	44.81	70.89	96.14	121.87	147.57	173.27	198.71
$\Sigma L_{cable}/\Sigma L_{truss}$	1.36	2.07	2.78	3.49	4.19	4.90	5.61
$\Sigma L_{cable}/\Sigma L_{truss}$	1.89	2.91	3.90	4.91	5.91	6.92	7.91
$\Sigma L_{cable}^&/\Sigma L_{cable}$	1.39	1.41	1.41	1.41	1.41	1.41	1.41

[Table 5.3] Total length of truss and cables used and their ratios (* Reference frame, &Special case)

5.3.3 Result and Discussion

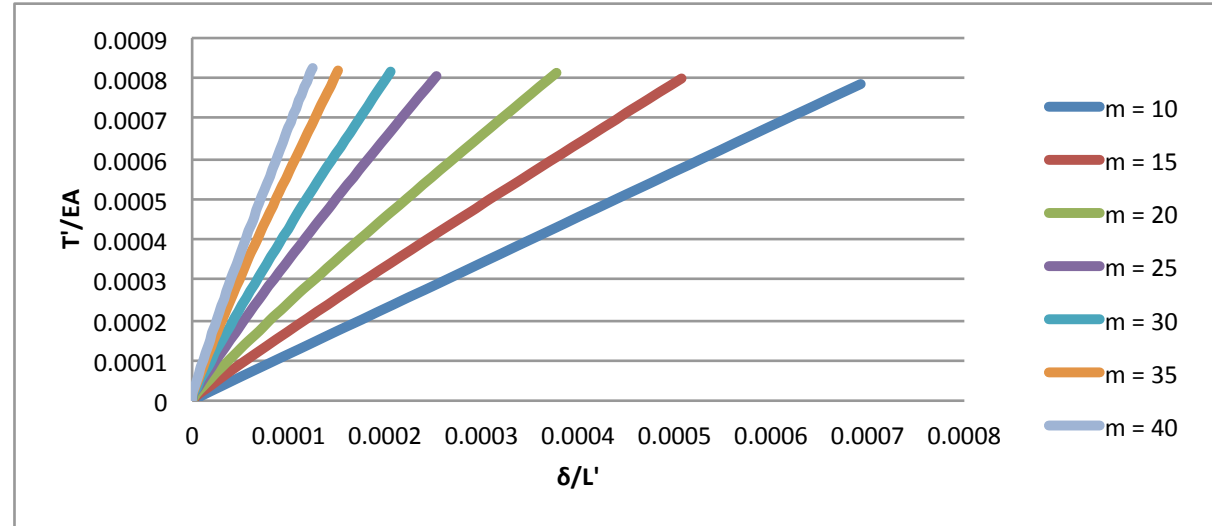


[Figure 5.16] Cable pre-strain (T'/EA) vs. axial strain (δ/L') for various m (Non-slide, Special)

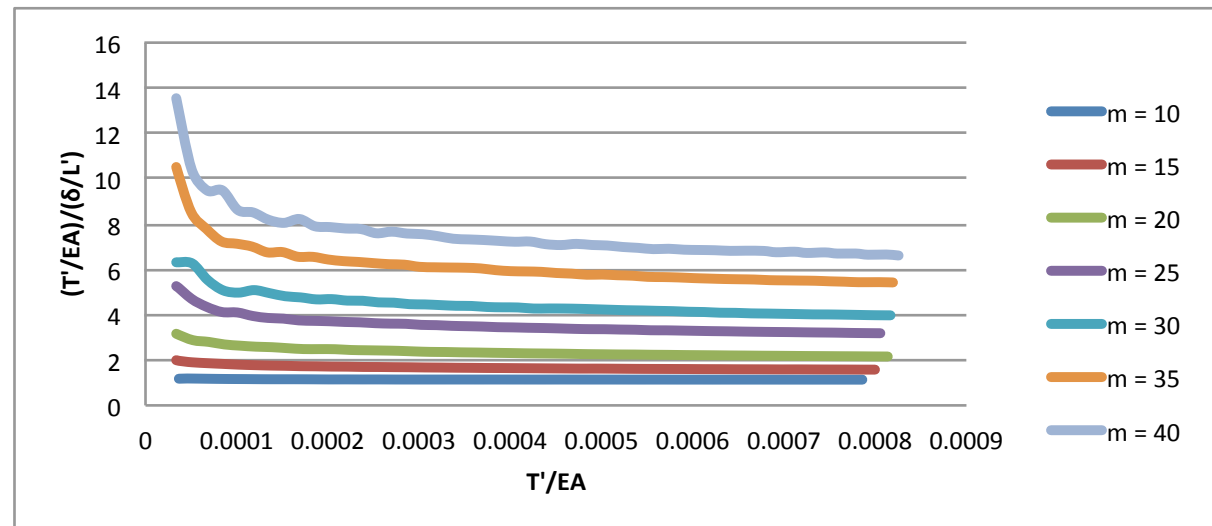


[Figure 5.17] Si $((T'/EA)/(\delta/L'))$ ratio vs. cable pre-strain (T'/EA) for various m (Non-slide, Special)

[Figure 5.16] and [Figure 5.17] shows a similar correlation consistent with the earlier findings for the ordinary case in [Test 2] although the gradient S_i $((T'/EA)/(\delta/L'))$ is much steeper for all cases of m . The ratios of maximum and minimum S_i for the special case of cable arrangement in [Figure 5.18] compared against the maximum and minimum for the ordinary case of cable arrangement confirm that the frame is far stiffer for the special case when $m^& > m$. There is also an increasing discrepancy between the ratios of S_i as m increases.

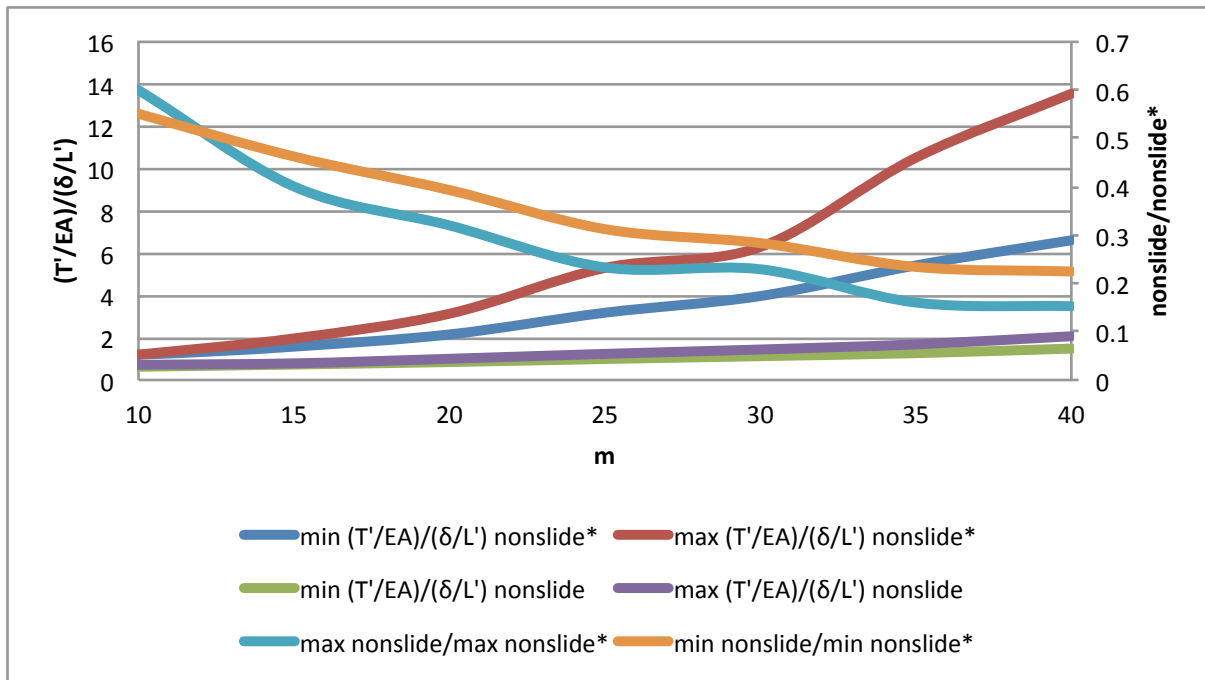


[Figure 5.18] Si $((T'/EA)/(\delta/L'))$ ratio vs. m (*Special case)

[Figure 5.19] shows a more uniform stress distribution throughout the cables in the frame for the special case than the ordinary case. With 41% more cable material required for the special case, the improvement in S_i could be attributed to a greater uniformity in the transfer of forces to the boundary truss for larger values of m .

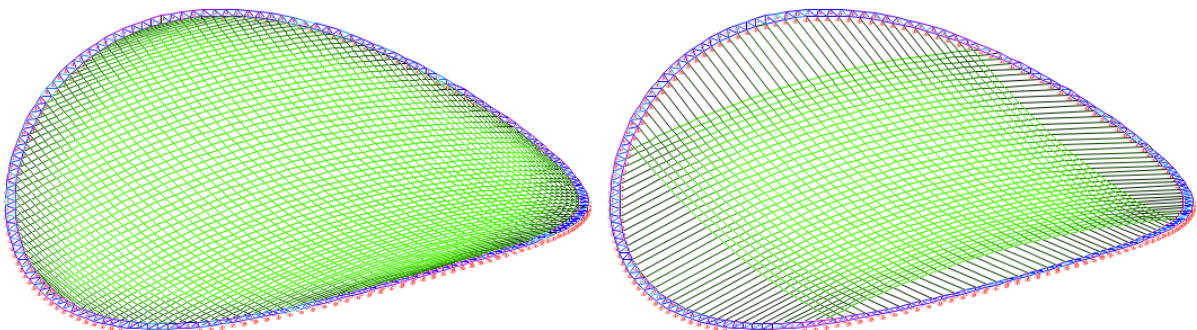


[Figure 5.19] Special $m=40$ (Left) vs. ordinary $m=40$ (Right) where stress (Max = Green, Min = Black)

Using an arch analogy, a partially or non-uniformly loaded arch deflects more. This is true for the ordinary form of cable arrangement where only a quarter of the overall frame is acted upon as shown in [Figure 5.20].

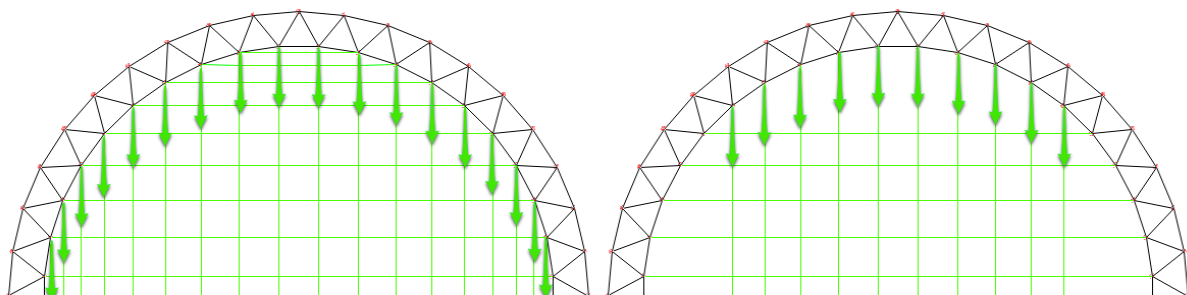


[Figure 5.20] Force acting on boundary truss for the special (Left) and the ordinary (Right) case ($m=10$)

In [Figure 5.21], the number of cables spanning from one quarter to the opposite quarter, $m = 16$ for the special case, and $m = 30$ for the ordinary case. However $m^* = 30$ for the special case as well.

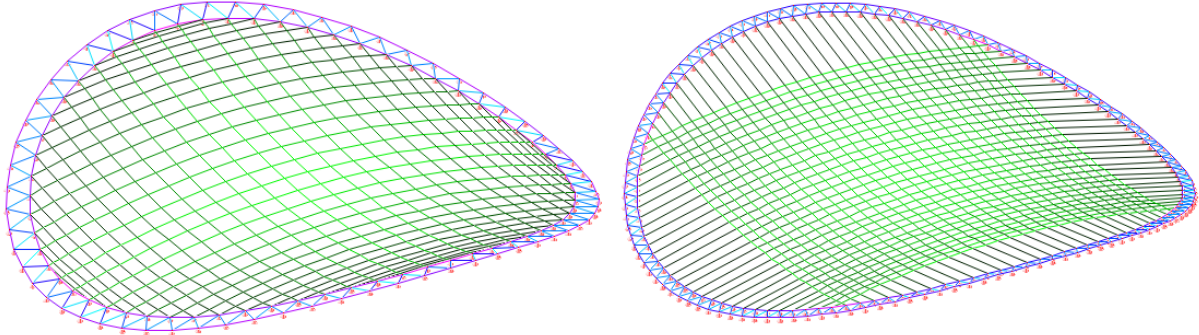


[Figure 5.21] Special $m=16$ (Left) vs. ordinary $m=30$ (Right) where stress (Max =Green, Min =Black)

Comparing the actual number of cables, the minimum S_i for the total number of cables have been plotted in [Figure 5.22] for both special and ordinary cases along with the ratio of their S_i . At best, the minimum S_i for the ordinary case is 60% that of minimum S_i for the special case and appears to continue being lower with increasing m .

Reading off [Figure 5.15] for the special case $m = 16$, the total length of cable required $\approx \text{span} \times 40$ whereas for ordinary case $m = 30$, the total length of cable required $\approx \text{span} \times 50$ as the arrangement of cables is denser towards the middle because of the greater distance between the opposite ends. The amount of truss material required is $\approx \text{span} \times 12$ for both as $r_o:r_i$ shrinks to compensate for a denser mesh of diagonal truss elements.

Hence, it can be concluded that as well as being more efficient in terms of cable material, the special case of cable arrangement is also stiffer than the ordinary form of cable arrangement.

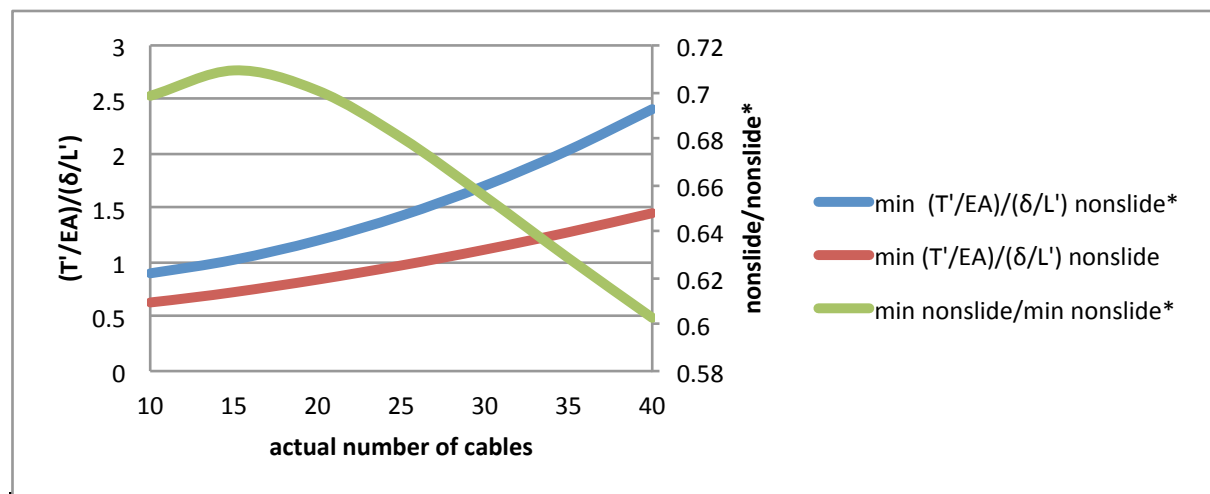


[Figure 5.22] $S_i ((T'/EA)/(\delta/L'))$ ratio vs. actual number of cables (*special case)

5.3.4 Limitations

The ratio of the truss cross sectional area to cable cross sectional area $A_{\text{truss}}:A_{\text{cable}}$ may influence the actual relationship between S_i and m as these results are only valid for the case when $A_{\text{truss}}:A_{\text{cable}} = 7.0$. However, the general trend is likely to hold true.

6 Conclusion

6.1 Summary

This investigation has attempted to understand the behaviour of ellipse plan hyperbolic paraboloid cable net structure - consisting of a boundary truss and a cable net grid - with varying parameters; predominantly how the pre-strain in the cables affects the axial strain of the structural frame. The following is a summary of the findings.

6.1.1 Test 1: Axial strain due to cable pre-strain and truss to cable x-sectional ratio

The greater the ratio of truss cross sectional area to cable cross sectional area, $A_{truss}:A_{cable}$, the greater the S_i , which is the ratio of cable pre-strain $\varepsilon_{i,cables}$ to axial strain of the frame along the major axes $\varepsilon_{i,frame}$, therefore the stiffer the frame. The failure of the structural frame is governed by the cable strength when $A_{truss}:A_{cable}$ is high and by the truss strength when $A_{truss}:A_{cable}$ is low. There is an optimum $A_{truss}:A_{cable}$ ratio where the full cross-sectional capacity of the truss and cable members are mobilised giving the stiffest structural frame for the highest cable pre-strain value. While the frame is very stiff when $\varepsilon_{i,cables}$ is small, the stiffness of the frame reduces as more ε_{cables} is applied due to the deformation of the geometry such that the mechanism that allows for a greater strain rate is activated slowing to a constant. When the cables are not allowed to slide, S_i is much greater compared to when they are allowed to slide. Therefore, the frame is stiffer axially due to a more even distribution of stresses in the cables. The lower the $A_{truss}:A_{cable}$ ratio, the greater the discrepancy between slide and non-slide configuration of cables. When $A_{truss}:A_{cable}$ is high, the ratio of slide and non-slide S_i configuration tends towards one.

6.1.2 Test 2: Axial strain due to cable pre-strain and the number of cables

The greater the number of cables per quarter, m , the greater the S_i , and so the stiffer the frame. Also with increasing m , the discrepancy between slide and non-slide configuration of cables is greater. When there are fewer cables, the distinction between slide and non-slide case becomes negligible.

6.1.3 Test 3: Axial strain due to special case of cable arrangement

The special case of cable arrangement is more or less uniformly loaded and has greater S_i , so is therefore much stiffer than the ordinary form of cable arrangement, which deflects more due to partial loading. As m increases, greater uniformity in load transfer to the boundary leads to further improvement in S_i , with higher discrepancy compared to the ordinary case of cable arrangement. When comparing a frame with a special case of cable arrangement and a lower m against an ordinary frame with same number of cables but a greater m , the special case is stiffer and uses 20% less cable material for the given configuration of geometry.

6.2 Further Investigation

6.2.1 Effect of varying the elastic modulus of cable and truss material

While the investigation into how varying the truss and cable cross sectional area ratio has already provided some insight into how the change in relative stiffness of the cables and truss members affects the way the structural frame deforms, a quantifiable relationship between the ratio of truss and cable elastic moduli with the ratio of cable pre-strain and axial strain was not covered which could be further looked into as a follow up to the work initiated here.

6.2.2 Effect of varying aspect ratio and curvature ratio

The aspect ratio of the frames investigation were all $a_x : a_y = 1:1$. Other aspect ratios may have different deformation mechanisms that affect the way axial displacements occur, which could help inform a designer of the consequences of choosing differing aspect ratios. The findings of this investigation are based on curvature ratio of $b_x : b_y : b_z = 1:1:0.15$. The effect of varying the curvature could also be interesting.

6.2.3 Effect of loading the frame and temperature effects

While the attempt to quantify the effect of pre-stress has been made for a frame of the outlined geometrical configuration, there is still an opportunity to understand the effect of loading the frame in the direction normal to gravity to determine the flexural stiffness for a combination of load cases, e.g. UDL to simulate dead load from insulation panels; live load due to wind or snow load; or a point impact load. Partial loading on one half of the structure, which is known to induce higher moment and deflection in arches, is a problem that could be translated and applied to the geometry presented here to determine if it is also the worst possible case for the proposed geometry and to quantify it. The extent of how change in temperature affects the geometry and distribution of stresses in the cables is also a possible avenue of exploration.

There is also a scope for producing a relaxation algorithm that identifies the initial shape of the frame before any pre-stress or vertical loading is applied when the final shape of the frame is known. The algorithm implemented in the software written for this investigation is only applicable to the problem of identifying the initial shape of the frame before any pre-stress is applied.

6.2.4 Effect of pre-strain on maximum stresses experienced by the members

It is to be acknowledged that the effect of cable pre-strain on the effective stresses realised by the cable and truss members has not been delved into in detail. A study into this could help establish an interchangeable relationship between the cable pre-strain and the magnitude of maximum tensile and compressive stresses experienced by the members. Ways to reduce them could be looked at by focusing on the members where the maximum stresses are, understanding why they occur and determining the area of the cross sections or other means to give a stress distribution as close to the defined stress distribution as possible from selection of viable options.

6.2.5 Comparison of the results with a physical model

While this investigation sheds some light on how the structural frame behaves in a computational environment, comparing the results against a physical model could help verify the results and understand phenomena that have perhaps not been considered.

6.3 Final Comments

This investigation provides an insight into the behaviour of ellipse plan hypar frame with a free truss boundary and cable net grid. The results are significant in understanding how the structure behaves when the relative stiffness of the cables compared to the truss varies. The results also help understand the behaviour of the frame when it increases in complexity with increasing number of cables constrained geometrically. The results also highlight the differences due to the form of cable arrangement. The modified dynamic relaxation algorithm implemented to carry out the analysis in terms of determining the unknown initial geometry from the known final geometry and unknown final stress distribution from the known initial stress distribution is also of significance that could be applied to problems of a similar nature.

Bibliography

- Barnes, M. (1994). Form and stress engineering of tension structures. *Structural Engineering Review*, 6, 175-202.
- Berger, H. (1996). *Light structures - structures of light*. Basel: Birkhauser.
- Bletzinger, K.-U., Wüchner, R., Daoud, F., & Camprubi, N. (1998). *Form Finding and Optimization of Membranes and Minimal Surfaces*. Lyngby: Technical University of Denmark.
- Buchholdt, H. (1999). *An introduction to cable roof structures* (2nd ed.). London: Thomas Telford.
- Clarke, J. H. (2011). The Hyperbolic Paraboloid as an Approximation to a Surface of Minimal Area. *Architectural Science Review*, 9 (2), 53-54.
- Colding, T. H., & Minicozzi, W. P. (2006, June 2). Shapes of embedded minimal surface. (R. C. Kirby, Ed.) Cambridge: Massachusetts Institute of Technology.
- Day, A. S. (1965). Introduction to dynamic relaxation. *The Engineer*, 219-221.
- Design Quarterly. (1969). Frei Otto. *Process and Imagination* (74/75), 25-27.
- Dill, E. H. (2007). *Continuum Mechanics: Elasticity, Plasticity, Viscoelasticity*. CRC Press.
- Lewis, W. J. (2003). *Tension Structures: Form and Behaviour*. Thomas Telford.
- Lewis, W., & Lewis, T. (1996). Application of Formian and Dynamic Relaxation to the Form Finding of Minimal Surfaces. *Journal of the IASS*, 37 (3), 165-186.
- Noddy, T. (2004, January 17). *Bubble Science*. Retrieved February 2, 2011 from Tom Noddy's Bubble Magic: <http://www.tomnoddy.com/science.html>
- Olympic Delivery Authority. (2011, February 22). *London 2012 Velodrome – construction complete*. Retrieved February 3, 2012 from London 2012: <http://www.london2012.com/documents/oda-publications/velo-complete-final.pdf>
- Osserman, R. (1986). *A Survey of Minimal Surfaces*. New York: Dover.
- Otto, F., & Rasch, B. (1995). *Finding Form* (A ed.). Menges: Deutscher Werkhund Bayern.
- Plateau, J. (1873). *Experimental and Theoretical Statics of Liquids*. (K. Brakke, Trans.) London: Trubner and Co.
- Scheck, H. (1974). The force density Method for form finding and computation of general networks. *Computer Methods in Applied Mechanics and Engineering*, 3, 115-134.
- Seward, D. (2003). *Understanding Structures* (3rd ed.). Michigan: Palgrave Macmillan.
- Southern, R. (2011). *The Force Density Method: A Brief Introduction*. The National Centre for Computer Animation. Poole: Bournemouth University.
- Spivak, M. (1999). *A comprehensive introduction to differential geometry* (3rd ed., Vol. 1). Houston, Texas: Publish or Perish Inc.

Struik, D. J. (1961). *Lectures on Classical Differential Geometry* (2nd ed.). Reading: Addison-Wesley Publishing Company, Inc.

Tenu, V. (2009). *Minimal surfaces as self-organizing systems*. University College London, Bartlett School of Graduate Studies. London: University College London.

Tibert, G. (1999). *Numerical Analyses of Cable Roof Structure*. Department of Structural Engineering. Royal Institute of Technology.

Williams, C. J. (2001). The analytic and numerical definition of the geometry of the British Museum Great Court Roof. (M. Burry, S. Datta, A. Dawson, & A. Rollo, Eds.) *Mathematics and Design*, 434-440.

Williams, C. J. (2003, July 7). *The definition of curved geometry for widespan enclosures*. Retrieved February 5, 2012 from Chris William Home Page: <http://people.bath.ac.uk/abscjkw/OrganicForms/WideSpan.pdf>

Williams, C. J. (n.d.). *The Maud Algorithm*. Retrieved 03 12, 2012 from University of Bath: <http://people.bath.ac.uk/abscjkw/MaudAlgorithm/Maud.pdf>

Zhang, Y., & Tabarrok, B. (1999). Generation of surfaces via equilibrium of forces. *Computers and Structures*, 70 (6), 599-613.

Appendix

Note on result data

The test results for each of the tests are submitted in the archive folder attached to this document. If they are not available and would like to request a copy, please email b.kunwar@gmail.com. They are organised logically into folders referring to the respective test such that,

	Test 1	Test 2	Test 3
Non-slide	t=2,4,6,8,10,12,14,16	m=10,15,20,25,30,35,40	m=10,15,20,25,30,35,40
Slide	t=2,4,6,8,10,12,14,16	m=10,15,20,25,30,35,40	N/A

Note on source code

The source code used for analysis is attached with this submission. If it is not available or your version does not work, please email b.kunwar@gmail.com requesting a copy.

To run the code, it may be necessary to install the latest version of:

1. “Java” available from <http://www.java.com>
2. “Processing” software from <http://www.processing.org>

The following files are contained within a code folder “Velodrome” both of which must be present in the folder in order for the code to be functional:

1. VelodromeQ.pde
2. Output.pde